Phosphate Induces a Morphological Shift that Enhances Vascular Dissemination of *Cryptococcus neoformans*

Steven T. Denham[1], Brianna Brammer[1], Krystal Y. Chung[1], Morgan A. Wambaugh[1], Joseph Bednarek[1], Li Guo[1], and Jessica C.S. Brown[1,2*]

[1]Division of Microbiology and Immunology, Department of Pathology, University of Utah, Salt Lake City, UT 84112, USA

[2]Lead Contact

[*]Correspondence: jessica.brown@path.utah.edu

SUMMARY:

Phenotypic heterogeneity is a common microbial strategy to improves fitness in fluctuating environments. The fungal pathogen *Cryptococcus neoformans* exhibits dramatic size heterogeneity: it varies from 2-100 µm in diameter during mammalian infection. Following pulmonary invasion, cells enlarge to >30 µm diameter, then decrease over disease course. Extrapulmonary organs, particularly the brain, contain uniformly small cells, implying that that morphotype is important for dissemination. To test this hypothesis, we isolated size-based *ex vivo* cell populations directly from mouse lungs. Small *ex vivo* cells readily disseminated compared with other *ex vivo* populations, small beads, and *in vitro*-grown small cells. The latter two groups are close in size to small *ex vivo* cells, suggesting that while size is important, fungal-specific elements also drive extrapulmonary dissemination. We found that mannose exposure facilitates host cell interaction and organ uptake. Phosphate induces small cell formation. This demonstrates how environmental cues shift phenotypic heterogeneity to drive pathogenesis.

INTRODUCTION:

Phenotypic heterogeneity within microbial populations promotes fitness in fluctuating and complex host environments (Weigel and Dersch, 2018). Heterogeneity arises among isogenic microbial populations as cells communicate, divide labor, and stochastically alter gene expression. Microbial responses to host microenvironments can also lead to phenotypic heterogeneity, even within single foci of infection (Davis, 2018). For example, microbial cells at the perimeter of infection foci may be more open to attack from immune cells, while the core may be depleted of nutrients and oxygen (Davis et al., 2015; Kowalski et al., 2019). Phenotypic heterogeneity can also influence which cells in a localized population are more likely to spread to new sites within a host, a phenomenon that significantly impacts the likelihood and trajectory of cancer metastasis (San Juan et al., 2019). However, due to the bottlenecks involved, we

36 understand little about how phenotypic heterogeneity influences the spread of infectious
37 microbes within a host.
38 In this study, we used the model human fungal pathogen *Cryptococcus neoformans* to
39 address the role that phenotypic heterogeneity plays in intra-host dissemination. A ubiquitous
40 saprophytic fungus associated with trees and bird guano (Emmons, 1955; Lazéra et al., 1996),
41 *C. neoformans* is generally harmless, with human exposure thought to be as high as 70% by
42 age five (Goldman et al., 2001). Infection follows inhalation of a fungal cell or spore (Maziarz
43 and Perfect, 2016), and in immunocompromised individuals *C. neoformans* disseminates via the
44 bloodstream and/or lymphatics to almost any organ in the body (Lin et al., 2015; Maziarz and
45 Perfect, 2016). *C. neoformans* cells rapidly proliferate in the central nervous system, and the
46 resulting fungal meningoencephalitis drives cryptococcosis patient mortality, killing ~180,000
47 people each year worldwide (Rajasingham et al., 2017).
48 *C. neoformans* is an excellent model organism to study the impact of phenotypic
49 heterogeneity on intra-host dissemination. Two of its primary virulence attributes—cell and
50 capsule size—vary considerably during infection and are readily observable via microscopy and
51 flow cytometry (Li and Nielsen, 2017). Isolates belonging to the *Cryptococcus* genus exhibit a
52 high degree of cell and capsule size diversity, and morphological heterogeneity strongly impacts
53 *C. neoformans* virulence: increased capacity for morphological variation among isolates
54 correlates with worse clinical outcome (Fernandes et al., 2018).
55 Cell and capsule size are finely tuned to a multitude of environmental signals and impact
56 stress resistance, immune recognition, and overall pathogenesis (Casadevall et al., 2019;
57 O'Meara and Alspaugh, 2012). Cells grown in nutrient replete laboratory media are
58 morphologically homogenous (5–10 μm in total (cell + capsule) diameter) and poorly
59 encapsulated (O'Meara and Alspaugh, 2012), while fungal cells proliferating in the lungs are
60 morphologically heterogeneous (1-100 μm in total diameter) and encapsulated, although
61 capsule thickness varies considerably (Wang and Lin, 2015; Zaragoza, 2011). In the host, the
62 polysaccharide capsule shields immunostimulatory microbe-associated molecular patterns in
63 the fungal cell wall, suppresses phagocytosis, and protects against oxidative stress (Casadevall
64 et al., 2019; O'Meara and Alspaugh, 2012).
65 The best understood *C. neoformans* morphotype is the polyploid (≥4C) “titan” cell,
66 measuring 10-100 μm in cell body diameter (Dambuza et al., 2018; Hommel et al., 2018;
67 Okagaki and Nielsen, 2012b; Okagaki et al., 2011; Trevijano-Contador et al., 2018; Zaragoza et
68 al., 2010; Zhou and Ballou, 2018). Titans are more resistant to phagocytosis and oxidative

69 stress and skew immunity toward a non-protective Th2 response (Crabtree et al., 2012; Okagaki
70 and Nielsen, 2012b; Okagaki et al., 2010).
71 While titans contribute considerably to cryptococcal pathogenesis, they are not the only
72 morphotype present during infection, accounting for a minority of cryptococcal cells within the
73 lungs (Zhou and Ballou, 2018). Tissue-specific differences in cryptococcal morphology also
74 manifest in human patients and animal infection models (Denham et al., 2017; Rivera et al.,
75 1998; Xie et al., 2012). Titan cells are rarely observed outside of the lungs, and overall cell and
76 capsule sizes tend to be substantially smaller in extrapulmonary sites, including the brain
77 (Charlier et al., 2005; Denham et al., 2017; Rivera et al., 1998; Xie et al., 2012). We previously
78 observed that median cell and capsule size within the lungs of mice inoculated with the highly
79 virulent KN99 strain of *C. neoformans* decreased from >30 μm to ~10 μm over the course of
80 infection, correlating with extrapulmonary dissemination (Denham et al., 2017). Thus, we
81 hypothesize that smaller morphotypes are more likely to disseminate.
82 Most infection models—including intravenous dissemination models—use *C.*
83 *neoformans* yeast cells collected from nutrient replete laboratory media as the inoculum, failing
84 to capture the phenotypic heterogeneity generated during lung infection (Mukaremera et al.,
85 2019; Ngamskulrungroj et al., 2012b; Sabiiti et al., 2012). In this study, we accounted for
86 phenotypic heterogeneity generated during lung infection by isolating cells directly from infected
87 lung tissue and sorted them according to size. We then intravenously challenged naïve mice
88 with those freshly isolated cryptococcal cells to determine the influence of morphology on
89 bloodstream dissemination.
90
91 **RESULTS:**
92
93 ***Cryptococcus* strain-dependent morphological transitions during pulmonary infection**
94 **correlate with dissemination.**
95 *Cryptococcus* spp. isolates vary in their capacity for morphological variation (Fernandes
96 et al., 2018). To more broadly assess morphological shifts during infection, we inoculated ~8-
97 week-old female B6 mice with a panel of common *Cryptococcus* spp. reference strains (2.5×10^4
98 cells / mouse). At 3 days post-inoculation (dpi) and 17 dpi, we homogenized lungs and
99 measured fungal cell body and capsule size (**Figures 1A and 1B**). Morphogenesis varied
100 widely among *Cryptococcus* isolates. While KN99 (*C. neoformans*) and Bt63 (*C. neoformans*)
101 cells shifted smaller between 3 and 17 dpi, R265 (*C. deuterogattii*) and WM276 (*C. gattii*)
102 continued to increase in size—largely due to increased capsule thickness. Smaller median cell

103 size at 17 dpi correlated with increased extrapulmonary burden (**Figures 1C and 1D**). These
104 data suggest that among *Cryptococcus* isolates, the emergence of small cells (<10 μm) within
105 the lungs is a strong predictor of extrapulmonary dissemination.
106 We also measured cell and capsule size in the blood, liver, spleen, and brains of mice
107 inoculated with KN99 cells (**Figure 1E**). The range of cell size in the blood and liver was
108 surprisingly broad considering that murine microcapillaries can be as small as 3.5 μm. Although
109 rare, we did find fungal cells in the blood measuring 50 μm across. However, median total
110 diameter in the blood at 17 dpi was 12.72 μm, which was noticeably smaller than earlier
111 timepoints in the lungs (27.21 μm at 3 dpi and 18.71 μm at 14 dpi) indicating that entry into the
112 blood may still be a size-limiting bottleneck. In contrast, cell size in the spleen and brain was far
113 more restricted. The vast majority of cells in the spleen were <15 μm, while cells in the brain
114 rarely exceeded 10 μm in total diameter. These data suggest that the cell/capsule size profile
115 generated within the lungs is a strong predictor of extrapulmonary dissemination, and that
116 multiple bottlenecks may restrict vascular dissemination.
117
118 **Inoculum size alters the rate at which *C. neoformans* populations shift toward smaller**
119 **cell size in the lungs and disseminate to the brain.**
120 Lower initial cell density increases the frequency of titan cell formation *in vitro* (Trevijano-
121 Contador et al., 2018) and *in vivo* (Okagaki et al., 2010). We hypothesized that reducing the
122 number of cells in the inoculum would increase the frequency of larger cells early in lung
123 infection and slow the rate of small cell formation (**Figures S1A, S1B, and S1C**). We inoculated
124 mice with 10^3, 10^4, or 10^5 KN99-mCherry cells / mouse and employed the flow cytometry
125 forward scatter-area (FSC-A) parameter as a high-throughput assay to estimate relative
126 changes in cell size at 3, 7, 10, 14, and 17 dpi.
127 Consistent with our hypothesis, inoculating mice with fewer fungal cells increased fungal
128 cell size at 3 dpi, decreased the rate of cell size reduction in the lungs (**Figures S1A, S1B, and**
129 **S1C**), decreased lung fungal burden (**Figure S1D**), and decreased dissemination to the brain at
130 17 dpi (**Figure S1E**). Therefore, lower initial fungal cell density slows the rate at which fungal
131 cells shift smaller in the lungs and disseminate to the brain.
132
133 **Populations of cells isolated from the lungs according to size display differences in their**
134 **cell surface features and are differentially bound by soluble host factors.**
135 When we compared the labor-intensive microscopy-based measurements of cell size
136 with flow cytometry-based measurements, we still observed a fungal size shift over the course

137 of infection (**Figure S1A**). Thus, we sought to isolate KN99-mCherry cells from infected lung
138 tissue (14 dpi) via fluorescence-activated cell sorting (FACS) according to size (FSC-A),
139 characterize them, and directly test their ability to disseminate through the vasculature. We
140 sorted cross-sections of the fungal cell size distribution corresponding to the smallest (small *ex*
141 *vivo*: median total diameter of 7.56 μm), middle (mid *ex vivo*: median total diameter of 14.04
142 μm), and largest (large *ex vivo*: median total diameter of 21.80 μm) ~20% of the population
143 (**Figure 2A**). We further confirmed that we isolated distinct populations based on cell and
144 capsule size (**Figure 2B**) and that fungal cells sorted from each gate were also equivalently
145 viable (**Figure 2C**).
146 In addition to the differences in cell and capsule size among the three populations, we
147 observed differences in DNA ploidy measured by 4′,6-diamidino-2-phenylindole (DAPI) staining
148 (**Figure 2D**). Haploid cells cultured in minimal yeast nitrogen base (YNB) medium +/- benomyl
149 served as controls for 1C and 2C DNA content; benomyl inhibits cell division, trapping cells at
150 2C. Cells with >2C content are considered titan cells. Only the large *ex vivo* population
151 contained an appreciable number of titan cells (mean: 21.4% >2C) (**Figure S2**). Mid *ex vivo*
152 cells averaged 74.2% 1C and 22.8% 2C, while small *ex vivo* cells averaged 89.2% 1C and
153 10.0% 2C.
154 Morphological changes in *C. neoformans* are often accompanied by alterations in cell
155 surface architecture and immune recognition. We screened the binding rate (% total fungal cells
156 bound) of a panel of soluble receptors to small, mid, and large *ex vivo* cells (**Figure 2E**). Large
157 *ex vivo* cells were more likely to be bound by complement protein C3 than mid, or small *ex vivo*
158 cells. In contrast, small and mid *ex vivo* cells were more likely to be bound by lung surfactant
159 protein D (SPD). SPD binding to *C. neoformans* is deleterious for the host, potentially because
160 SPD agglutinates fungal cells and disrupts fungal clearance by macrophages (Geunes-Boyer et
161 al., 2012). We saw uniform and low-level binding of IgA and IgM class antibodies, and little to no
162 binding by mannose-binding lectins.
163 Differences in host factor binding suggested that cell surface architecture may differ
164 among the sorted populations. We used two lectins to probe the exposure of microbial features
165 in different layers of the cell wall: wheat germ agglutinin (WGA), which recognizes chitin in the
166 inner-most layers of the cryptococcal cell wall and concanavalin A, which binds mannose on
167 mannoproteins in the outer cell wall and inner capsule. There were no significant differences in
168 chitin exposure as measured by flow cytometry (**Figure 2F**). However, mannose was
169 significantly more exposed on small *ex vivo* cells compared with mid and large *ex vivo* cells and
170 cells grown in non-capsule inducing minimal YNB medium (**Figure 2G**).

171 We visualized mannose exposure pattern via microscopy and characterized staining as
172 negative, punctate (one or more distinct staining puncta), diffuse (staining covers the observable
173 cell surface), or both punctate and diffuse (**Figure 2H**). Mannose was more likely to be exposed
174 both at specific puncta and diffusely across the surface of small *ex vivo* cells. Mannose
175 exposure can correspond to recent bud scars, which may explain the punctate staining in our
176 analysis (Panepinto et al., 2007). The high prevalence of diffuse mannose exposure on small
177 cells may be due to their relatively thin capsules. Altogether, these results suggest that cell and
178 capsule size heterogeneity correlates with heterogeneity in cell surface architecture and
179 immune recognition.
180
181 **Small *ex vivo* cells disseminate to extrapulmonary organs at a higher rate than mid and**
182 **large *ex vivo* cells.**
183 To directly address the impact of fungal cell and capsule size on dissemination, we
184 intravenously inoculated naïve mice with small, mid, and large *ex vivo* cells (10^5 cells / mouse).
185 With blood flow from the tail vein running directly to the heart and then lungs for reoxygenation,
186 the lungs harbor the first major bed of microcapillaries fungal cells are likely to encounter
187 following tail vein inoculation. Therefore, sorting fungal cells from infected lung tissue prior to
188 tail vein inoculation roughly replicates the fate of fungal cells had they entered the bloodstream
189 from the lungs. Consistent with our hypothesis, a greater number of small *ex vivo* cells reached
190 the liver, spleen, and brain by 3 hours post-inoculation (hpi) than mid and large *ex vivo* cells
191 (**Figure 3A**). In contrast, the majority of mid and large *ex vivo* cells remained in the lungs at 3
192 hpi, possibly because they failed to navigate the lung microcapillaries as well as small *ex vivo*
193 cells. We observed the same trends in fungal burden at 3 dpi, indicating that small *ex vivo* cells
194 are well-capable of proliferating in extrapulmonary tissues (**Figure 3A**).
195 Although brain fungal burden was equivalent in mice inoculated with mid and large *ex*
196 *vivo* cells at 3 hpi, there were more mid *ex vivo* cells in the brain by 3 dpi. We asked whether the
197 reduced brain fungal burden in mice inoculated with large *ex vivo* cells was due to inefficient
198 blood-brain barrier crossing or reduced proliferation in the brain. To estimate blood-brain barrier
199 crossing *in vivo*, we intracardially perfused mice at 3 hpi to drive out circulating fungal cells and
200 normalized the fungal burden in perfused mice to nonperfused mice inoculated on the same
201 day. While perfusion did not significantly affect brain fungal burden in mice inoculated with small
202 or mid *ex vivo* cells, perfusion drove nearly all of the large *ex vivo* cells from the brain (**Figure**
203 **3B**). In contrast, fungal burden post-intracranial inoculation was independent of initial fungal cell

204 size (**Figure 3C**), suggesting that while large *ex vivo* cells are poorer at reaching the brain and
205 crossing the blood-brain barrier, they are not deficient at proliferating in the brain.
206
207 **Macrophages, but not platelets or neutrophils, clear small *ex vivo* cells from the**
208 **vasculature to reduce brain dissemination.**
209 As small *ex vivo* cells most efficiently disseminated to extrapulmonary organs, we
210 examined the mechanisms governing their dissemination profile more closely. Most small *ex*
211 *vivo* cells that made it past the lungs at 3 hpi were cleared in the liver and spleen (**Figure 3A**).
212 The liver plays a major role in clearing microbes and microbial components from the blood
213 (Macpherson et al., 2016). Recently, intravital imaging revealed that liver macrophages clear *C.*
214 *neoformans* cells from the blood stream (Sun et al., 2019). However, the inoculum for those
215 studies consisted of *C. neoformans* cells cultured *in vitro*. Our cell surface characterization
216 revealed that small *ex vivo* cells differ from cells cultured *in vitro* (YNB medium), mid *ex vivo*,
217 and large *ex vivo* cells, which may influence liver macrophage recognition of *C. neoformans*
218 cells.
219 To address the role of macrophages in clearing small *ex vivo* cells from the bloodstream,
220 we depleted macrophages from the liver, spleen, and bone marrow of mice with clodronate
221 liposomes 48 hours prior to inoculation (**Figures S3A and S3B**). Macrophage depletion reduced
222 small *ex vivo* cell fungal burden in the liver, while increasing fungal burden in the lungs, kidneys,
223 and brain at 1 dpi (**Figure 3D**). These results corroborate the findings of Sun *et al*, in that liver
224 macrophages play a critical role in filtering *C. neoformans* from the blood (Sun et al., 2019).
225 However, we also found that small *ex vivo* cells grow rapidly in the liver compared with *in vitro*-
226 grown cells or other *ex vivo* populations (**Figure 3E**), suggesting that attempts by the host to
227 clear *C. neoformans* cells by sequestering them in the liver may backfire.
228 Besides macrophages, platelets and neutrophils are among the most abundant immune
229 cell-types present in the blood that contribute to microbial clearance. Platelets can recognize
230 either complement protein bound to microbes or microbial features directly to initiate microbial
231 clearance, especially in the spleen (Broadley et al., 2016). Platelets don't appear to interact with
232 encapsulated *C. neoformans*, or mediate the clearance of *in vitro*-grown *C. neoformans* cells
233 from the blood (Sun et al., 2019). We also did not see any effect on fungal dissemination when
234 platelets were depleted prior to inoculation with small *ex vivo* cells (**Figures S4A, S4B, and**
235 **S4C**).
236 It's unclear whether neutrophils play a predominantly protective or detrimental role
237 during cryptococcosis, though there is evidence neutrophils can clear *C. neoformans* from the

238 blood (Sun et al., 2016; Zhang et al., 2016). In an intravenous infection model using *in vitro*-
239 grown fungal cells as the inoculum, neutrophil depletion greatly increased fungal burden in the
240 lungs and brain (Sun et al., 2016; Zhang et al., 2016). However, neutrophil-depletion prior to
241 inoculation with small *ex vivo* cells slightly increased lung fungal burden, but did not affect
242 fungal burden in other organs, indicating that the small *ex vivo* cells are more resistant to
243 neutrophil-mediated clearance than typical *in vitro*-grown fungal cells (**Figures S4D, S4E, and**
244 **S4F**).
245
246 **Macrophage recognition of small *ex vivo* cells is partially mediated by mannose**
247 **exposure.**
248 We predicted that liver macrophages may recognize the high levels of exposed
249 mannose on the surface of small *ex vivo* cells. We isolated liver macrophages from healthy ~8-
250 week-old B6 mice (Li et al., 2014) and co-cultured them with 6 µm plastic beads, minimal (YNB)
251 medium-grown cells, and sorted *ex vivo* populations at a multiplicity of infection of 2:1. Half of
252 the wells also received pretreatment with exogenous mannan, with the prediction that it would
253 reduce macrophage association when mannan recognition is critical. After 4 hours we washed
254 away free fungal cells, leaving only the fungal cells bound or internalized by macrophages,
255 which we define as "macrophage association".
256 Approximately 60% of macrophages had associated with 6 µm plastic beads by 4 hours,
257 indicating that the liver macrophages still displayed phagocytic capacity *ex vivo* (**Figure 3F**).
258 Additionally, 17.67% of liver macrophages associated with small *ex vivo* cells, which was more
259 than twice the frequency of mid and large *ex vivo* cells. Pretreatment with exogenous mannan
260 prior to infection reduced macrophage association with small *ex vivo* cells by ~40%, but did not
261 affect association with mid and large *ex vivo* cells, YNB-grown cells, or beads. These data
262 suggest that liver macrophages recognize small *ex vivo* cells in part through exposed mannose,
263 and that mannose exposure could contribute to fungal clearance in the liver.
264 Liver macrophages and other macrophages that sample the bloodstream are subject to
265 shear force, which can affect recognition and phagocytosis of microbes and other foreign matter
266 (Broadley et al., 2016). We assessed whether mannose exposure on small *ex vivo* cells affects
267 vascular clearance *in vivo* by intravenously injecting either 400 µg of exogenous mannan or
268 vehicle (PBS) 2-3 minutes prior to intravenous inoculation with 10^5 small *ex vivo* cells. 10
269 minutes later, we perfused mice to drive out non-recirculating fungal cells and plated organs for
270 colony forming units to estimate fungal burden. If mannose recognition contributed to fungal
271 clearance in a given organ, we expected to see reduced fungal burden in mice that received

272 exogenous mannan, compared with the vehicle control. We repeated this experimental design
273 with additional fungal cell wall and capsule components (GXM, β-glucan, chitin), as well as
274 polyinosinic acid (poly(I)), which is a scavenger receptor ligand (Pearson et al., 1993).
275 Although mannan did reduce fungal clearance in the liver and kidneys by ~20% and in
276 the spleen by ~75% (**Figure 3G**), it was not the only fungal ligand that influenced vascular
277 clearance. Poly(I) reduced clearance to a strikingly similar extent as mannan. The purified
278 capsule polysaccharide GXM reduced clearance in a similar extent in the liver, spleen, kidneys
279 at roughly the same level (~40% reduction). β-glucan and chitin, on the other hand, did not
280 appreciably affect fungal clearance, possibly because of their buried position beneath the
281 capsule. These data indicate that clearance of small ex vivo cells is not dependent on a single
282 cell surface ligand and that there are tissue-specific dependencies on various fungal features
283 that mediate vascular clearance.
284
285 **Enhanced small *ex vivo* cell dissemination is not entirely dependent on size.**
286 We next assessed whether small *ex vivo* cells disseminate more efficiently due to their
287 size alone, or if there were other contributing factors. We inoculated mice via the tail vein with
288 either large *ex vivo* cells, small *ex vivo* cells or size-matched inert polystyrene beads. Large *ex*
289 *vivo* cells disseminated similarly to size-matched 25 μm beads; the majority resided in the lungs
290 at 3 hpi (**Figure 4A**). Additionally, more 6 μm beads disseminated past the lungs to reach the
291 liver and spleen compared with 25 μm beads. However, small *ex vivo* cells reached the liver and
292 spleen at an even higher frequency, indicating that absolute size influences fungal
293 dissemination through the vasculature, but it is not the only contributing factor.
294 We next examined *in vitro* conditions that could reproduce the small *ex vivo* cell
295 morphotype and dissemination profile. Previously, we observed that cells grown in capsule-
296 inducing medium (CAP) shifted toward smaller cell and capsule size if they were supplemented
297 with conditioned medium (CM) from cells grown in non-capsule inducing medium (yeast
298 nitrogen base + 2% glucose, or YNB) (Denham et al., 2017). YNB medium contains
299 vitamins, nitrogen, and glucose but not amino acids. YNB-grown cells suppress capsule
300 formation, and are typically <10 μm in diameter. CAP medium consists of 10% Sabouraud's
301 dextrose broth—made from digested animal tissue—buffered to pH 7.4. CAP medium induces
302 capsule growth and is sufficient for cell division. We collected CM by filtering supernatant from
303 saturated YNB-grown cultures. In this case, CM consists of unspent nutrients and soluble fungal
304 factors secreted during growth in non-capsule inducing conditions.

305 We compared the dissemination profile of small *ex vivo* cells to cells grown in three *in*
306 *vitro* populations: (1) YNB-grown cells (2) CAP-grown cells, and (3) CAP-grown cells
307 supplemented with CM (CAP+CM). We also subjected the *in vitro*-grown populations to the
308 same sorting process as *ex vivo* cells by sorting YNB, and CAP+CM-grown cells from the
309 "small" FSC-A gate (YNB cells: 5.64 μm median total diameter; CAP+CM cells: 6.48 μm median
310 total diameter; few YNB or CAP+CM cells fell in the "mid" or "large" FSC-A gates) and sorting
311 the CAP-grown cells from the "mid" FSC-A gate (12.11 μm median total diameter; few CAP-
312 grown cells fell into the "small" or "large" FSC-A gates) (**Figure 4B**).
313 The prior culture conditions and morphology of cells in the inoculum heavily impacted
314 dissemination. Only CAP+CM cells replicated the dissemination profile of small *ex vivo* cells in
315 terms of fungal burden at 3 hours and 3 days post-inoculation (**Figure 4C**). Despite being
316 roughly the same size as small *ex vivo* cells, YNB-grown cells displayed similar fungal burden to
317 CAP-grown cells at 3 hours, and lower fungal burden in extrapulmonary organs than CAP,
318 CAP+CM, and small *ex vivo* cells at 3 days. Therefore, both absolute fungal cell size, and the
319 physiological state of cells entering the blood influence the outcome of vascular dissemination.
320
321 **Cells sorted from infected host tissue or cells grown in host-like medium survive better**
322 **in the blood than cells grown in nutrient replete medium.**
323 The caveat to using fungal burden as a readout for dissemination is that we can't easily
324 distinguish between the ability of cells to reach certain organs, and their ability to survive. We
325 hypothesized that YNB-grown cells may not be as primed for survival in the bloodstream as
326 cells sorted from infected host-tissue or cells grown under stressful host-like conditions (CAP
327 medium).
328 To address that hypothesis, we examined the survival of *in vitro*- and *ex vivo*-sorted cells
329 in whole mouse blood, liver macrophage co-culture (multiplicity of infection of 1:1), and DMEM
330 as a medium control (96-well plates, 37 °C, 5% CO_2, static). We assessed fungal cell survival as
331 a percentage of input at 0-, 24-, and 48-hour timepoints. Liver macrophages suppressed *in vitro*
332 and *ex vivo* cell growth equivalently (**Figures 4D and 4E**). However, the *ex vivo* populations and
333 *in vitro* populations from host-like conditions survived better in blood than YNB-grown cells
334 (**Figure 4F**), with large and mid-*ex vivo* populations faring the best. These results support the
335 idea that size and physiology are critical for bloodstream dissemination: small *ex vivo* cells
336 combine the stress resistance required for increased survival in the blood with the smaller cell
337 size required for widespread dissemination via microcapillaries.
338

339 **Phosphate acquisition genes are upregulated in capsule-inducing medium and**
340 **suppressed following conditioned medium supplementation.**
341 CAP+CM-grown cells resemble small *ex vivo* cells in terms of cell + capsule size and
342 vascular dissemination profile, so we hypothesized that they might suitably model small cell
343 formation in the lungs. We analyzed the transcriptome of cells grown in YNB, CAP, and
344 CAP+CM medium to identify genes that might facilitate the transition to small cell size in host-
345 like capsule inducing conditions. We also analyzed the transcriptome of small, mid and large *ex*
346 *vivo* cells.
347 Comparing the transcriptome of CAP, CAP+CM, and the *ex vivo* populations to YNB-
348 grown cells demonstrated that the YNB-grown transcriptome is vastly different from each of
349 these populations (**Figure 5A**). Core sets of 699 and 291 genes were up- and down-regulated
350 respectively among the *ex vivo* populations and CAP/CAP+CM populations relative to YNB-
351 grown cells. There were also 1085 up-regulated and 1297 downregulated genes shared only
352 among the *ex vivo* populations relative to YNB-grown cells, demonstrating that the
353 transcriptome within the host environment is still quite distinct from even the host-like *in vitro*
354 conditions. Among the *ex vivo* populations, it is notable that small *ex vivo* cells were the most
355 transcriptionally distinct (**Figure S5A**). 928 genes were differentially expressed in small vs mid
356 *ex vivo* cells, and 2,365 genes were differentially expressed in small vs large *ex vivo* cells. For
357 comparison, only 93 genes were differentially expressed in mid vs large *ex vivo* cells (**Figure**
358 **S5A**).
359 Gene ontology term (GO-term) enrichment analysis revealed that phosphate ion
360 transport was upregulated in CAP-grown cells vs YNB-grown cells (**Figure 5C**), and
361 downregulated in CAP+CM vs CAP-grown cells (**Figure 5D**). In other words, phosphate
362 acquisition genes are induced when cells enter capsule-inducing conditions (CAP medium), and
363 then suppressed following supplementation with CM.
364 We observed the same trends when analyzing the expression of specific genes involved
365 in phosphate acquisition and storage (**Figure 5E**). When *C. neoformans* cells are starved of
366 phosphate, the phosphate acquisition transcription factor, Pho4, translocates to the nucleus
367 where it promotes its own gene expression and the expression of genes involved in phosphate
368 acquisition and storage. These include phosphate transporters: *PHO84*, *PHO89*, and *PHO840*;
369 phosphatases: *APH1* (secreted/vacuolar acid phosphatase) and *APH4* (predicted intracellular
370 acid phosphatase); and *VTC4* (vacuolar transport chaperone involved in processing
371 polyphosphate). Pho4-dependent genes were upregulated in CAP vs YNB-grown cells and then
372 suppressed in following CM supplementation—although many phosphate acquisition genes still

373 remained more highly expressed in CAP+CM-grown cells compared with YNB-grown cells.
374 Phosphate acquisition genes were also upregulated *in vivo* compared with YNB-grown cells,
375 suggesting that phosphate acquisition could be similarly linked to morphological shifts in the
376 host (**Figure 5E**).
377 Phosphate acquisition genes were also upregulated in the *ex vivo*-sorted populations
378 relative to YNB-grown cells, suggesting that the host lung environment is phosphate-limiting to a
379 degree. However, there were no differences in phosphate acquisition gene expression among
380 the three *ex vivo* populations. We limited our transcriptomic profiling of ex vivo cells to just one
381 timepoint (14 days post-inooculation). Had we profiled gene expression over time, we may have
382 observed changes more reflective of available phosphate concentrations in the lungs.
383
384 **Phosphate and acidic pH are sufficient to drive *C. neoformans* populations toward**
385 **smaller morphotypes following growth in alkaline and host-like conditions.**
386 We hypothesized that phosphate might be a critical nutrient that facilitates the
387 emergence of small cells in CAP+CM media. Conditioned medium consists of unspent YNB
388 medium and soluble fungal cell derived factors (Albuquerque et al., 2014). YNB medium is
389 defined, so we screened every component individually (including phosphate) to determine which
390 components are sufficient to induce small cell formation when cells are grown in CAP medium.
391 We also tested two soluble fungal-derived factors that accumulate during growth in YNB
392 medium: exo-GXM (Denham et al., 2017) and the quorum sensing-like peptide Qsp1 (Homer et
393 al., 2016; Lee et al., 2007).
394 We grew cells for 24 hours in YNB medium, then sub-cultured 10^5 cells/mL into CAP
395 medium for another 24 hours. We then sub-cultured CAP-grown cells 1:1 into fresh CAP
396 medium with 10% of the final volume being a YNB medium component, fungal-derived factor, or
397 water as the vehicle control. After a final 24-hour period, we measured cell size (FSC-A) by flow
398 cytometry.
399 Conditioned YNB medium and fresh YNB medium were sufficient to stimulate a shift
400 toward smaller cell size (**Figures 6A and 6B**). Among the YNB medium components, only
401 phosphate was sufficient to stimulate a shift toward smaller cell size (**Figure S5A**), and did so in
402 a concentration-dependent manner (**Figures 6A and 6B**). Phosphate-supplemented cells
403 decreased both total (cell+capsule) diameter (**Figure 6C**) as well as cell (**Figure S6A**) and
404 capsule (**Figure S6B**) size individually. Phosphate was also sufficient to induce a shift toward
405 smaller size for cells grown in titan cell-inducing medium (5% Sabouraud's, 10% fetal calf
406 serum, 15 μM sodium azide, pH 7.4, 5% CO_2, 37 °C) (**Figure S5B**).

407 We previously reported that exo-GXM may trigger the formation of smaller cells
408 (Denham et al., 2017). However, we were unable to reproduce those results (**Figure S5A**),
409 possibly due to differences in exo-GXM preparation, but more likely because we previously
410 solubilized exo-GXM in phosphate buffered saline. Qsp1 is a cell-density dependent signaling
411 peptide that suppresses the formation of titan cells (Trevijano-Contador et al., 2018). However,
412 the addition of Qsp1 did not affect cell size in this model (**Figures S5A and S5B**).
413 The Pho84 and Pho840 phosphate transporters are phosphate/H^+ symporters, and *C.*
414 *neoformans* therefore requires a proton gradient to efficiently transport phosphate into the cell
415 (Kretschmer et al., 2014). In alkaline pH, *C. neoformans* struggles to efficiently import
416 phosphate and upregulates phosphate acquisition machinery (Kretschmer et al., 2014; Lev et
417 al., 2017). *C. neoformans* releases metabolites that acidify the local microenvironment and
418 increase nutrient uptake (Himmelreich et al., 2003; Wright et al., 2002). For instance,
419 cryptococcomas in the brain acidify to levels as low as pH 5.5 (Himmelreich et al., 2003; Wright
420 et al., 2002).
421 We measured lung pH in mice inoculated with *C. neoformans* throughout infection, and
422 found that pH in the lungs decreased from ~7.4 to as low as ~6.3 between 3 and 17 dpi (**Figure**
423 **6D**). Phosphate did not induce significant shifts in FSC-A-measured cell size when CAP
424 medium was buffered to 6.3, potentially because phosphate availability in CAP medium buffered
425 to pH 6.3 is not as limiting as pH 7.4 (**Figures 6A and 6B**). However, we did measure a modest,
426 but significant decrease in total (cell+capsule) diameter when pH 6.3 CAP-grown cells were
427 supplemented with phosphate (**Figure 6C**), which was mostly due to a decrease in capsule
428 thickness (**Figure S5**). These data indicate that cell body and capsule size enlarge when
429 phosphate is limiting due to starvation, alkaline pH, or both. When phosphate availability
430 increases due to higher extracellular concentrations or decreased extracellular pH, *C.*
431 *neoformans* cells shift toward smaller morphotypes.
432
433 **Limiting phosphate acquisition genetically suppresses morphogenesis *in vivo*.**
434 Since phosphate was sufficient to trigger cell and capsule size reduction *in vitro*, we
435 hypothesized that limiting phosphate acquisition *in vivo* would alter morphogenesis, perhaps
436 delaying the appearance of small morphotypes. To test this hypothesis, we intranasally
437 inoculated mice with wild-type KN99, or either of two independently constructed KN99:*pho4*Δ
438 strains, which lack the gene encoding the transcription factor *pho4*. Without *pho4*, *C.*
439 *neoformans* cells fail to adequately upregulate genes involved in phosphate acquisition when
440 available phosphate is limiting, and become hypersensitive to alkaline conditions. The *pho4*Δ

441 mutant is attenuated for growth in the lungs but more severely attenuated for dissemination to
442 the brain, due to its poor survivability in alkaline blood (Lev et al., 2017). Our findings replicated
443 the work from Lev *et al.*, in that the *pho4*Δ mutant cells were attenuated for proliferation in the
444 lungs **(Figure 6E)** and dissemination to the brain **(Figure 6F)**. We also found that cell and
445 capsule size of *pho4*Δ mutant cells populating the lungs was static and less heterogeneous
446 relative to wild-type cells **(Figures 6G, S6C, and S6D)**. Most *pho4*Δ mutant cells remained
447 between 10 and 20 μm in total (cell + capsule) diameter over 17 days **(Figure 6G)**, with many of
448 them also exhibiting irregular budding **(Figures 6H)**. Total median wild-type (cell + capsule)
449 diameter was far larger than the *pho4*Δ mutant at day 3 (wild-type: 26.13 μm; *pho4*Δ #1: 14.55
450 μm; *pho4*Δ #2: 14.17 μm) and smaller than the *pho4*Δ mutant at day 17 (wild-type: 10.25 μm;
451 *pho4*Δ #1: 13.87 μm; *pho4*Δ #2: 15.10 μm), indicating that phosphate acquisition mediated by
452 *pho4* is required for the full range of fungal morphogenesis during infection, including the shift
453 toward smaller morphotypes **(Figure 6G)**.
454
455 **DISCUSSION:**
456 We found that phenotypic heterogeneity is dynamic and supports *C. neoformans*
457 dissemination from the lungs. Capsule growth and titan cell formation during early stages of
458 lung infection enhance fungal resiliency, and as fungal proliferation continues, smaller cells with
459 greater potential for extrapulmonary dissemination emerge and/or survive. These smaller
460 morphotypes are phenotypically and transcriptionally distinct and can more easily navigate
461 microcapillaries to reach sites such as the brain. To our knowledge, these experiments were the
462 first to directly test the influence of *in vivo*-generated phenotypic heterogeneity on *C.*
463 *neoformans* dissemination, and the first to analyze the transcriptome of discrete *C. neoformans*
464 subpopulations infecting the lungs.
465 *C. neoformans* morphology is important at multiple stages of disease progression. For
466 example, inhalation of spores rather than yeast cells may accelerate dissemination, because
467 dendritic cells more readily phagocytose spores and quickly traffic them to draining lymph nodes
468 (Walsh et al., 2019). Spores exhibit elevated pathogenicity compared to genetically identical
469 yeast cells (Walsh et al., 2019). On yeast cells, the degree of encapsulation also altered the
470 trajectory of disease progression through initial interactions with macrophages in a zebrafish
471 infection model (Bojarczuk et al., 2016). Titan cells, in addition to being resistant to
472 phagocytosis, decrease the phagocytosis of smaller cells, potentially facilitating smaller cells'
473 dissemination (Okagaki and Nielsen, 2012a).

474 The dynamics of phenotypic heterogeneity *in vivo* varied widely among *Cryptococus*
475 isolates. Isolates that shifted toward smaller morphotypes (KN99 and Bt63) exhibited greater
476 extrapulmonary fungal burden than isolates that remained morphologically static (52D) or those
477 that shifted toward larger morphotypes as disease progressed (R265 and WM276). Absolute
478 size is likely not the sole reason for the difference in dissemination among these isolates. For
479 instance, R265 cells shifted larger over the course of lung infection, but R265 cells also die
480 more quickly in blood than KN99 cells (Ngamskulrungroj et al., 2012b). The capacity for
481 morphological heterogeneity is likely more important than any given morphological feature, such
482 as capsule thickness, cell body size, or titan formation, as different morphologies will hold
483 advantages at different stages of disease progression (Fernandes et al., 2018), allowing for a
484 bet hedging strategy during infection.
485 Our data also indicate that size alone does not explain the disseminating ability of small
486 *ex vivo* cells. Namely, cells originating from more stressful environments such as host lungs or
487 host-like *in vitro* conditions were better primed for survival and dissemination *in vivo*. Poorly
488 encapsulated small cells grown in nutrient replete YNB medium survived worse in blood and
489 failed to disseminate as well as small encapsulated *ex vivo* cells or small encapsulated cells
490 generated *in vitro* (CAP+CM) (**Fig. 4**). This suggests that efficient bloodstream dissemination
491 requires that cryptococcal cells adopt smaller cell and capsule morphologies, along with stress
492 resistance that will prime them for survival in the blood (Alanio et al., 2015; Ngamskulrungroj et
493 al., 2012a). These findings will be important to consider when optimizing future models of fungal
494 dissemination.
495 Cell size heterogeneity correlates with heterogeneity in cell surface architecture. Smaller
496 cell body size correlated with thinner capsule size and greater mannose exposure *in vivo*. Prior
497 data supporting the importance of mannose recognition by the host during cryptococcosis is
498 contradictory. Mannose receptor deficient mice are more susceptible to *C. neoformans* infection
499 (Dan et al., 2008). However, mannose recognition was dispensable for murine, but not primary
500 human, macrophage phagocytosis of *C. neoformans and C. gattii* cells *in vitro* (Lim et al., 2018).
501 There is also conflicting evidence as to whether mannose-binding lectin (MBL) deficiency
502 predisposes individuals to cryptococcal infection (Eisen et al., 2008; Fang et al., 2015). Despite
503 the increased mannose exposure on small *ex vivo* cells, we did not see significant MBL-binding
504 to cryptococcal cells. This may be due to the fact that MBL is most abundant in serum, and we
505 analyzed fungal cells from perfused lung tissue. We did find increased surfactant protein D
506 (SPD) binding of small and mid *ex vivo* cells compared with large *ex vivo* cells, and SPD can
507 bind to mannose-rich microbial features (Sahly et al., 2002). Our results indicate that the

508 importance of mannose recognition depends on a given fungal cell's morphotype: the addition of
509 exogenous mannan reduced macrophage association with small *ex vivo* cells, but not large *ex*
510 *vivo* cells or small YNB-grown cells. Increased mannose exposure may actually present a fungal
511 cell fitness cost that comes with reduced size. Smaller capsules and more recent bud scarring
512 may leave more mannose (and potentially other) residues exposed for recognition by
513 phagocytes.

514 Nutrient availability, particularly phosphate, is sufficient to shift toward smaller cell and
515 capsule morphologies. Out of all the YNB medium components, only phosphate was sufficient
516 to induce the shift toward smaller cell and capsule size *in vitro*. Also, suppressing phosphate
517 acquisition by deleting the *pho4* gene limited phenotypic heterogeneity *in vivo*: neither large nor
518 small morphotypes appeared in mouse lungs. Phosphate is essential for cell homeostasis and
519 growth, and its acquisition is tightly controlled in microbes that absorb fluctuating levels of
520 phosphate from their surroundings (Köhler et al., 2020; Lev and Djordjevic, 2018). Phosphate is
521 also critical for *Candida albicans* morphogenesis (hyphal formation), stress resistance, and
522 tissue invasion (Ikeh et al., 2016; Liu et al., 2018).

523 Phosphate acquisition is also essential for survival in the blood and dissemination to the
524 brain (Lev et al., 2017). *Cryptococcus* relies on a proton gradient to import many different
525 nutrients, including phosphate, into the cell (Lev and Djordjevic, 2018). Thus, *C. neoformans*
526 survives poorly in the alkaline (pH 7.4) bloodstream when its ability to upregulate phosphate
527 acquisition machinery is impaired (Lev et al., 2017). Our results suggest that increased
528 phosphate availability also impacts dissemination at an even earlier stage by mediating the
529 emergence of small *C. neoformans* morphotypes within the lungs. We observed an order of
530 magnitude decrease in lung pH over the course of infection, which could also enhance
531 acquisition of phosphate and other nutrients (Lev et al., 2017) or independently repress capsule
532 growth (Farhi et al., 1970; O'Meara and Alspaugh, 2012).

533 Since *pho4* mutants cannot form either large or small cells *in vivo*, it leads to the
534 question of whether small cells are daughters of large cells such as titans. Zhou *et al* (Zhou et
535 al., 2020) reported small cells, termed "titanides," that are titan daughter cells. We can obtain
536 small cells *in vitro* without inducing titan cells beforehand (**Fig. 6**). Since phosphate-induced
537 small cell formation is pH-dependent (**Fig. 6A-C**), there could be multiple pathways for small cell
538 formation. Moreover, cell division is required for small cell formation *in vitro*, since if we do not
539 add fresh growth medium when inducing small cells *in vitro*, the population size does not shift
540 (**Fig. 6B**). In other ways, titanides are similar to our "small" cells, particularly their hypothesized
541 roll in dissemination. Small cells are also about the same size as "drop" cells (Alanio et al.,

542 2015). These cells are of similar size as small cells but were isolated due to high non-
543 cytoplasmic levels of the glutathione stain CMFDA, which measures oxidative stress response,
544 and are not viable (Alanio et al., 2015).

545 Many studies identify fungal cell ploidy as a key driver of adaptation, in-host survival,
546 pathogenicity (Gerstein et al., 2015; Okagaki and Nielsen, 2012b; Selmecki et al., 2015). Of our
547 *ex vivo* populations, only large cells contain >2N cells (**Fig. S2**), and even within the large cell
548 population, the majority of cells are 2N, which could be either cells in the G2 phase of mitosis or
549 smaller titan cells. Medium cells display the DNA content profile of actively growing haploid
550 yeast cells (Todd et al., 2018). Thus, we think that comparisons between small and medium *ex*
551 *vivo* cells are likely independent of ploidy.

552 There are some notable limitations to our study. For example, we did not define the
553 subpopulations within the lungs based on clear biological criteria, but rather sorted cross-
554 sections of the population of fungal cells proliferating within the lungs. Small *ex vivo* cells
555 correspond with the size of disseminated cells in the brain, but medium and large cells are
556 based on arbitrary size cutoffs designed to distinguish them from small cells. Clearer definitions
557 of fungal subpopulations within the lungs and analysis of their dissemination would greatly
558 enhance our understanding of systemic cryptococcosis. For example, multiple groups have also
559 documented the appearance of unusually small "micro" (~1 μm), sometimes tear-dropped
560 shaped cells *in vivo* that are somewhat similar in shape to the small ex *vivo* cells in this study
561 (Feldmesser et al., 2001; Fernandes et al., 2018; Zaragoza, 2011). Properties of these "micro-
562 cells" are largely unknown and they could be very young, metabolically dormant, or aneuploid
563 cells (Dambuza et al., 2018; Feldmesser et al., 2001; Fernandes et al., 2018; Zaragoza, 2011).
564 Despite limited characterization, they likely represent the smallest cryptococcal cells seen
565 during infection. Though some of the cells sorted from infected lung tissue did present these
566 phenotypes, we did not attempt to further classify micro-cells.

567 Furthermore, *C. neoformans* faces multiple bottlenecks during dissemination, including
568 escaping the lungs. *C. neoformans* can escape the lung mucosa to access the bloodstream by
569 crossing lung epithelial cells, or via the Trojan horse mechanism within macrophages (Denham
570 and Brown, 2018). We focused on extrapulmonary organ entry rather than examining lung
571 escape by smaller cells directly. However, our small cells are more likely to be phagocytosed,
572 which may lead to increased Trojan horse dissemination. We also find that in late infection (17
573 dpi), the total diameter of cells in the blood shows a size distribution similar to the lungs (**Fig.
574 1E**), suggesting that pulmonary escape may be less of a bottleneck than previously thought.

575 Phosphate was sufficient to induce size reduction of *C. neoformans* cells. Since
576 phosphate is released from damaged cells (Gabow et al., 1982), we propose that small cells
577 could form as a progressing *C. neoformans* infection damages the host tissue, thus priming the
578 invading fungi for dissemination as tissue barriers are breaking down. Conditioned and fresh
579 YNB medium induced a greater size shift than phosphate alone, particularly at pH 6.3.
580 Combinations of different nutrients may also be sufficient to induce a size shift. Shifts toward
581 smaller cell and capsule size can be mediated by signals in addition to nutrient availability. For
582 example, Zhao *et al*. recently demonstrated that alleviation of genotoxic stress, such as that
583 seen during immune-mediated oxidative bursts, activates meiosis genes in polyploid titan cells
584 such that they begin to bud smaller haploid cells (Zhao et al., 2020).
585 Overall, we determine that a small, phosphate-inducible morphotype impacts a critical
586 step in *C. neoformans* pathogenesis: dissemination from the lungs to the brain. Our results are
587 consistent with observations in humans (Fernandes et al., 2018), in that phenotypic
588 heterogeneity strongly influences clinical outcome. Small *C. neoformans* cells are found in the
589 brains of human patients with cryptococcal meningitis (Xie et al., 2012). The emergence and/or
590 survival of smaller morphotypes within the lungs results in a subpopulation of fungal cells
591 primed for vascular dissemination that survival in the blood and are better able to enter organs
592 than their larger counterparts..
593
594 **ACKNOWLEDGEMENTS:**
595 This work was supported by research grant R01AI130248 from the National Institutes of
596 Health to J.C.S.B. S.T.D. was supported by grant T32AI055434 from the National Institutes of
597 Health. Flow cytometry work was supported by the University of Utah Flow Cytometry Facility
598 through the National Cancer Institute Award Number 5P30CA042014-24 and by the National
599 Center for Research Resources of the National Institutes of Health under Award Number
600 1S10RR026802-01. RNA sequencing and analysis was performed by the High-Throughput
601 Genomics and Bioinformatics Analysis Facility, a part of the Huntsman Cancer Institute at the
602 University of Utah. Generation of the *pho4*Δ #1 clone was constructed in the Madhani laboratory
603 with support from National Institutes of Health funding (R01AI100272). We would also like to
604 thank Dr. Kyla Ost for her valuable input regarding the analysis of opsonin-binding via flow
605 cytometry. We would also like to thank Dr. Matthew Rondina and Dr. Alicia Eustes for their
606 assistance with *in vivo* platelet depletion.
607
608 **AUTHOR CONTRIBUTIONS:**

609 S.T.D. and J.C.S.B. conceived and designed the experiments. S.T.D., B.B., K.Y.C., and
610 M.A.W. performed the experiments. S.T.D., B.B., and J.C.S.B. analyzed the data. S.T.D. and
611 J.C.S.B. wrote the paper. S.T.D., B.B., K.Y.C., M.A.W., and J.C.S.B. edited the paper.
612
613 **DECLARATION OF INTERESTS:**
614 The authors have no competing interests to declare.
615
616 **Figure 1: Morphological transitions during pulmonary infections correlate with fungal**
617 **dissemination. (A)** Total (cell+capsule) diameter, cell body diameter, and capsule thickness
618 measurements at 3 and 17 days post-intranasal inoculation (dpi) of mice (Mann-Whitney U test;
619 N=4 mice per timepoint, 57-65 fungal cells measured per mouse at 3 dpi and 117-266 fungal
620 cells per mouse at 17 dpi). Solid lines in the violin plots indicate the median and dotted lines
621 mark quartiles. **(B)** Representative India ink images of fungal cells quantified in 1A. **(C)** Fungal
622 burden in mice at 17 dpi (One-way ANOVA and uncorrected Fisher's LSD). The bar graph
623 represents the mean. **(D)** Nonlinear regression of mean extrapulmonary (liver+spleen+brain)
624 fungal burden and median total (cell+capsule) diameter. **(E)** Total diameter in KN99-infected
625 lungs at 3, 10, and 14 dpi and total diameter in KN99-infected organs at 17 dpi (Mann-Whitney
626 U-test; N=4 mice per timepoint; fungal cells measured per mouse in the lungs: 275, blood: 38,
627 liver: 72, spleen: 43, brain: 72). Solid lines in the violin plots indicate the median and dotted lines
628 mark quartiles. All panels in Figure 1: ns: not significant *$p<0.05$; **$p<0.01$; ***$p<0.001$;
629 ****$p<0.0001$.
630
631 **Figure 2: Sorting and characterization of fungal populations from infected lungs. (A)**
632 FACS gating scheme for sorting KN99-mCherry cells from infected mouse lungs into
633 populations of "small", "mid", and "large" cells using forward scatter-area (FSC-A) to
634 approximate size. **(B)** Representative India ink images of cells sorted from "small", "mid", and
635 "large FSC-A gates and cell/capsule size measurements (N=97-120 fungal cells). Solid lines in
636 the violin plots indicate the median and dotted lines mark quartiles. **(C)** Cell viability post-sort
637 quantified by colony-forming unit (CFU) count (N=4). **(D)** Representative flow plot of DNA-
638 content measured with DAPI staining. YNB (minimal YNB medium). **(E)** Percentage of total cells
639 bound by complement (C3), surfactant protein D (SPD), mannose binding lectins A and C (MBL-
640 A; MBL-C), IgA, and IgM. **(F)** Representative flow plots and quantification of wheat-germ
641 agglutinin (WGA) stained cells to determine chitin exposure. **(G)** Representative flow plots and
642 quantification of concanavalin A (ConA) stained cells to determine mannose exposure. **(H)**

643 Representative images and characterization of mannose exposure pattern after staining with
644 ConA (N=50 fungal cells). All comparisons in Figure 2 were analyzed using one-way ANOVA
645 and uncorrected Fisher's LSD (ns: not significant; *p<0.05; **p<0.01; ***p<0.001; ****p<0.0001).
646 All bar graphs display the mean.
647
648 **Figure 3: Small *ex vivo* cells disseminate to extrapulmonary organs at a higher rate than**
649 **larger cells, with mannose recognition by macrophages contributing to their clearance**
650 **from the vasculature. (A)** Fungal burden, measured by colony forming unit counts (CFU), at 3
651 hours post-inoculation (hpi) and 3 days post-inoculation (dpi) in mice intravenously-inoculated
652 with small, mid, or large *ex vivo* cells (One-way ANOVA and uncorrected Fisher's LSD). **(B)**
653 Fungal burden in mice inoculated with sorted *ex vivo* fungal cells and perfused at 3 hpi. Fungal
654 burden was normalized to inoculated, but non-perfused control mice (Mann-Whitney U-test). **(C)**
655 Fungal burden at 3 dpi in mice intracranially inoculated with sorted *ex vivo* fungal cells (One-
656 way ANOVA and uncorrected Fisher's LSD). **(D)** Fungal burden at 1 dpi in mice pretreated with
657 either clodronate or vehicle control (PBS) liposomes and then inoculated with small *ex vivo* cells
658 and (Unpaired t test). **(E)** Fungal burden in the livers of mice (N=4-6) inoculated with *ex vivo*
659 fungal cells or fungal cells harvested from minimal YNB (YNB) medium at 3 and 72 hpi. Points
660 indicate the mean and the error bars indicate standard deviation. **(F)** Percentage of primary
661 cultured murine liver macrophages with physically associated plastic beads or fungal cells
662 (stained with Direct Yellow 96) after 4 hours. Dashed lines indicate 10-minute pretreatment with
663 exogenous mannan (One-way ANOVA and uncorrected Fisher's LSD; N=2263-3197 total
664 macrophages counted across 3 independent replicates). **(G)** Fungal burden in mice
665 intravenously treated with indicated ligand 2-3 minutes prior to intravenous inoculation with
666 small *ex vivo* fungal cells. Mice were perfused 10 minutes post-inoculation and fungal burden
667 was normalized to vehicle (PBS) treated controls (Unpaired t-test; N=6 mice per group). All
668 panels: ns: not significant *p<0.05; **p<0.01; ***p<0.001; ****p<0.0001. All bar graphs display
669 the mean.
670
671 **Figure 4: Small cells generated under host-like conditions *in vitro* replicate the**
672 **dissemination profile of small *ex vivo* cells. (A)** Percentage of total plastic beads or live cells
673 in the indicated organ 3 hours post-intravenous inoculation (hpi). **(B)** Representative India ink
674 images and quantification of cell and capsule size (N=100 fungal cells). YNB (minimal YNB
675 medium); CAP (capsule inducing medium); CAP+CM (capsule inducing medium supplemented
676 with 10% conditioned medium). **(C)** Fungal burden, measured by colony forming units (CFU), in

677 mice at 3 hpi. and 3 days post-inoculation (dpi). **(D)** Fungal cell survival in Dulbecco's modified
678 Eagle's medium (DMEM) and **(E)** liver macrophage co-culture (multiplicity of infection of 1:1)
679 measured as a percentage of input. **(F)** Fungal cell survival in mouse blood measured as a
680 percentage of input. All comparisons in Figure 4 were analyzed using one-way ANOVA and
681 uncorrected Fisher's LSD (*p<0.05; **p<0.01; ***p<0.001; ****p<0.0001). All bar graphs display
682 the mean.
683
684 **Figure 5: Expression of phosphate acquisition genes correlate with cell and capsule size**
685 **changes *in vitro* and are upregulated *in vivo*. (A)** Venn diagram of genes upregulated or
686 downregulated in different conditions relative to YNB-grown cells (YNB: minimal YNB medium;
687 CAP: capsule-inducing medium; CAP+CM: capsule inducing medium supplemented with 10%
688 conditioned medium). **(B)** Comparisons of the total number of differentially regulated genes
689 among *in vitro*-grown populations. **(C)** Top-ten most significantly enriched gene ontology (GO)
690 terms representing genes upregulated in CAP vs YNB-grown cells (-log10 (p-value)). Phosphate
691 ion transport was #46. **(D)** Top-ten most significantly enriched GO-terms representing genes
692 downregulated in CAP+CM vs CAP-grown cells (-log10 (p-value)). **(E)** Select phosphate
693 acquisition and storage RNA-seq gene expression relative to YNB-grown cells (adjusted p
694 values; *p<0.05; **p<0.01; ***p<0.001; ****p<0.0001). All bar graphs display the mean and error
695 bars the standard deviation.
696
697 **Figure 6: Phosphate is sufficient to drive *C. neoformans* toward smaller morphotypes in**
698 **alkaline host-like conditions and is required for morphogenesis *in vivo*. (A)** Cell size
699 measured using flow cytometry forward scatter (FSC-A) after growth in CAP-medium and
700 supplementation with the indicated factor (YNB: minimal YNB medium; CAP: capsule-inducing
701 medium; CAP+CM: capsule inducing medium supplemented with 10% conditioned medium).
702 FSC-A median fluorescence intensity (MFI) was normalized to control (10% H_2O)-treated cells
703 (one-way ANOVA and uncorrected Fisher's LSD). Bar graphs display the mean. **(B)**
704 Representative flow cytometry plots for conditions in Figure 6A. **(C)** Total (cell+capsule)
705 diameter measurements representing conditions in Figure 6A (Mann-Whitney U-test; N=200
706 fungal cells). Solid lines in the violin plots indicate the median and dotted lines mark quartiles.
707 **(D)** pH in *C. neoformans* strain KN99-infected and mock-infected mouse lungs at 3, 10, and 17
708 days post-inoculation (dpi) (N=4 mice; one-way ANOVA and uncorrected Fisher's LSD; error
709 bars represent standard deviation). All panels: ns: not significant *p<0.05; **p<0.01; ***p<0.001;
710 ****p<0.0001. **(E)** Lung fungal burden in mice at 3, 10, and 17 dpi (One-way ANOVA and

711 uncorrected Fisher's LSD). The bar graph represents the mean. **(F)** Brain fungal burden in mice
712 at 17 dpi (One-way ANOVA and uncorrected Fisher's LSD). The bar graph represents the
713 mean. **(G)** Total (cell+capsule) diameter measurements at 3, 10, and 17 dpi of mice (Mann-
714 Whitney U test; N=6 mice per timepoint; 50, 100, and 150 wild-type cells measured per mouse
715 at days 3, 10, and 17 respectively. 50, 50, and 100 *pho4*Δ mutant cells measured per mouse at
716 days 3, 10, and 17 respectively). **(H)** Representative India ink images of fungal cells quantified
717 in 6G.
718
719 **Supplemental Figure 1: Inoculum size alters the rate at which *C. neoformans* populations**
720 **shift toward smaller cell size in the lungs and disseminate to the brain. (A)** We inoculated
721 mice with the indicated number of KN99-mCherry cells. The line graph shows the forward
722 scatter-area (FSC-A) measurements at the indicated days post-inoculation (dpi), which
723 estimates relative fungal size in the lungs (N=6 mice per timepoint). Points indicate the mean
724 and the error bars indicate standard deviation. **(B)** Representative flow cytometry plots from
725 mice inoculated with 10^4 KN99-mCherry cells / mouse. **(C)** Quantification of the area under the
726 curve for the curves displayed in Figure S1A. Bar graphs display the mean fluorescence
727 intensity and error bars indicate standard deviation. **(D)** Lung fungal burden in the same mice
728 described in Figure S1A and quantified by colony forming units (CFU). **(E)** Brain fungal burden
729 in mice at 17 dpi quantified by CFUs. Bar graphs display the mean. All comparisons in Figure
730 S1 were analyzed using one-way ANOVA and uncorrected Fisher's LSD (ns: not significant;
731 *p<0.05; **p<0.01; ***p<0.001; ****p<0.0001).
732
733 **Supplemental Figure 2: DNA content of *ex vivo C. neoformans* populations.** Percentage of
734 cells with 1C, 2C, and >2C DNA content in the indicated population. Values correspond to the
735 representative flow cytometry plot in Figure 2D. Bar graphs display the mean.
736
737 **Supplemental Figure 3: Macrophage depletion efficiency in the liver and spleen. (A)**
738 Representative flow cytometry plots displaying the frequency of $CD45^+$, $F4/80^+$ macrophages in
739 the liver and spleen after treatment with either PBS (control) liposomes or clodronate liposomes.
740 **(B)** Quantification of macrophage depletion measured as the ratio of macrophages in
741 clodronate-treated mice to PBS-treated mice.
742
743 **Supplemental Figure 4: Depletion of platelets or neutrophils does not affect the**
744 **dissemination of small *ex vivo* cells. (A)** Fungal burden in mice, measured by colony forming

745 units (CFU), following treatment with PBS (control) or anti-GPIbα antibody to deplete platelets
746 prior to intravenous inoculation with 10^5 small *ex vivo* cells / mouse. **(B)** Platelet count (K: units)
747 in the blood before and after treatment with PBS (control) or anti-GPIbα antibody. **(C)**
748 Quantification of platelet depletion in Figure S4B. **(D)** Fungal burden in mice treated with PBS
749 (control) or anti-Ly6G antibody to deplete neutrophils prior to intravenous inoculation with 10^5
750 small *ex vivo* cells / mouse. **(E)** Representative flow cytometry plots displaying the frequency of
751 $CD45^+$, $Ly6C^+$, $Ly6G^+$ neutrophils in the blood after treatment with either PBS (control) or anti-
752 Ly6G antibody. **(F)** Quantification of neutrophil depletion measured as the ratio of neutrophils in
753 anti-Ly6G antibody-treated mice to PBS-treated mice. All comparisons in Figure S4 were
754 analyzed using unpaired t-tests (ns: not significant *p<0.05; **p<0.01; ***p<0.001;
755 ****p<0.0001). All bar graphs display the mean.
756
757 **Supplemental Figure 6: Screen for factors that induce cell size reduction. (A)** Fungal cell
758 size measured by forward scatter-area (FSC-A). Cells were cultured in capsule inducing
759 medium (CAP medium) buffered to pH 7.4 or 6.3 before subculture (1:1) in fresh medium with
760 10% of the final volume being the indicated supplement solubilized in H_2O (CM: conditioned
761 medium; GXM: glucuronoxylomannan; YNB: minimal YNB medium; PBS: phosphate buffered
762 saline). **(B)** Fungal cell size measured by forward scatter-area (FSC-A) of cells cultured in titan
763 cell medium and subcultured as described in Figure S5A. All comparisons in Figure S5 were
764 analyzed using one-way ANOVA and uncorrected Fisher's LSD (ns: not significant; *p<0.05;
765 **p<0.01; ***p<0.001; ****p<0.0001). All bar graphs display the mean and error bars indicate
766 standard deviation.
767
768 **Supplemental Figure 5: Phosphate acquisition genes are upregulated in *ex vivo*-sorted**
769 **cells. (A)** Comparisons of the total number of differentially regulated genes among *ex vivo*-
770 sorted populations. **(B)** Select phosphate acquisition and storage RNA-seq gene expression
771 relative to YNB-grown cells (adjusted p values; *p<0.05; **p<0.01; ***p<0.001; ****p<0.0001). All
772 bar graphs display the mean and error bars the standard deviation.
773
774 **Supplemental Figure 7: Phosphate is sufficient to induce cell body diameter and capsule**
775 **thickness reduction in alkaline capsule-inducing medium and is required for**
776 **morphogenesis *in vivo*. (A)** Cell body diameter and **(B)** capsule thickness of cells cultured in
777 capsule inducing medium (CAP medium) buffered to pH 7.4 or 6.3 before subculture (1:1) in
778 fresh medium with 10% of the final volume being the indicated supplement solubilized in H_2O

779 (CM: conditioned medium; YNB: minimal YNB medium). Solid lines in the violin plots indicate
780 the median and dotted lines mark quartiles. All comparisons in Figure S6 were analyzed using
781 Mann-Whitney U-tests; N=200 fungal cells (ns: not significant; *p<0.05; **p<0.01; ***p<0.001;
782 ****p<0.0001). **(C)** Cell body diameter and **(D)** capsule thickness measurements at 3, 10, and
783 17 days post-intranasal inoculation (dpi) of mice (Mann-Whitney U test; N=6 mice per timepoint;
784 50, 100, and 150 wild-type cells measured per mouse at days 3, 10, and 17 respectively. 50, 50,
785 and 100 *pho4*Δ mutant cells measured per mouse at days 3, 10, and 17 respectively).
786
787
788 **METHODS:**
789
790 **Fungal strains and growth media**
791 The following strains were used in this study: KN99α (Brown lab stock which was also
792 the background for mutant strains), Bt63 (Brown lab stock, NCBI:txid1295841), 52D (ATCC
793 24067), R265 (ATCC MYA4093), WM276 (ATCC MYA-4071).
794 The following growth media were used in this study: YNB medium (yeast nitrogen base
795 without amino acids [Difco catalog no. 291940], 2% glucose), CAP medium (10% Sabouraud's
796 dextrose [Difco catalog no. 238230], buffered with 50 mM HEPES (pH 7.4) or MES (pH 6.3)),
797 Titan cell medium (5% Sabouraud's dextrose, 10% fetal calf serum (GenClone catalog no. 25-
798 550), 15 μM sodium azide, 50 mM HEPES (pH 7.4)).
799 To screen for factors that facilitated shifts in cell size, we picked single colonies from *C.*
800 *neoformans* cells streaked on YPAD agar and cultured them overnight (12-18 hours) in YNB
801 medium at 30 °C. We then sub-cultured those cells into YNB medium, CAP medium, or titan cell
802 medium for 24 hours at an initial cell density of 10^5 cells/mL. YNB- and CAP-grown cells were
803 cultured at 37 °C, while titan cell medium-grown cells were cultured at 37 °C and 5% CO_2. At
804 this stage, conditioned medium (CM) was collected from the 24-hour YNB cultures by pelleting
805 the fungal cells and filtering (0.22 μm pore size) the supernatant. 450 μl of the CAP and titan
806 cell media cultures were sub-cultured into 450 μl fresh media and 50 μl (10% of the final
807 volume) of one of the following supplements solubilized in H_2O: 10% H_2O (vehicle control), CM,
808 1% CM, 50 μg GXM, 50 μM Qsp1 peptide (Peptide 2.0: NFGAPGGAYPW), 50 μM Qsp1
809 scrambled peptide (Peptide 2.0: AWAGYFPGPNG), 10% 1XPBS (phosphate-buffered saline),
810 10% YNB medium; the following YNB medium supplements were added to a final concentration
811 that equaled their concentrations in YNB medium: 2% glucose, 4.531 nM folic acid, 8.186 nM
812 biotin, 250.6 nM copper sulfate pentahydrate, 531.4 nM riboflavin, 602.4 nM potassium iodide,

813 839.5 nM calcium pantothenate, 971.3 nM Sodium molybdate dihydrate, 1.186 μM thiamine
814 hydrochloride, 1.233 μM ferric chloride hexahydrate, 1.458 μM p-aminobenzoic acid, 1.945 μM
815 pyridoxine hydrochloride, 2.477 μM zinc sulfate heptahydrate, 2.649 μM manganese sulfate
816 monohydrate, 3.249 μM niacin, 8.087 μM boric acid, 11.10 μM inositol, 901.1 μM calcium
817 chloride dihydrate, 1.711 mM sodium chloride, 4.154 mM magnesium sulfate heptahydrate,
818 7.348 mM potassium phosphate monobasic, and 37.8mM ammonium sulfate. The
819 supplemented cultures were incubated for another 24 hours at 37 °C, following which 400 μl
820 was aliquoted to estimate cell size by flow cytometry and another 400 μl was aliquoted to
821 measure cell and capsule size (see "fungal cell size measurements") in India ink (Higgins
822 catalog no. 44201).
823
824 **Mouse infection models and fungal burden analysis**
825 For intranasal inoculations, ~8-week-old female C57BL/6NJ mice (Jackson Laboratory)
826 mice were anesthetized with ketamine/dexmedetomidine hydrochloride (Dexdomitor) delivered
827 intraperitoneally. They were then suspended by their front incisors on a horizontal strand of
828 thread. Unless otherwise indicated, mice were inoculated intranasally with $2.5x10^4$
829 *Cryptococcus* cells in 50 μl of 1XPBS using a micropipette. The inoculum was placed dropwise
830 onto a nasal flare before being inhaled by mice. Ten minutes later, mice were intraperitoneally
831 administered the reversal agent atipamezole (Antisedan).
832 For intravenous inoculations, ~8-week-old female C57BL/6NJ mice (Jackson
833 Laboratory) were warmed under a heat lamp before being placed in a restraint. Mice were
834 inoculated via the tail vein with 10^5 *C. neoformans* cells or beads in 200 μl of 1XPBS using 28-
835 gauge x 12.7 mm syringes. In order to competitively inhibit host interactions with fungal
836 components *in vivo*, we administered 400 μg of GXM (see "GXM isolation), mannan (Sigma-
837 Aldrich catalog no. M7504), β-glucan (Millipore Sigma catalog no. 1048288), the chitin monomer
838 N-acetyl glucosamine (Vector Laboratories S-9002), or polyinosinic acid (Poly(I)) (Sigma-Aldrich
839 catalog no. 26936-41-4) in 200 μl of 1XPBS 2-3 minutes prior to inoculation with fungal cells.
840 For intracranial inoculations, ~6-week-old female C57BL/6NJ mice (Jackson
841 Laboratories) were anesthetized with ketamine/dexmedetomidine hydrochloride as described
842 above. They were inoculated intracranially with 10^3 *C. neoformans* cells in 30 μl of 1XPBS via a
843 26-gauge 1/2-inch needle. Following inoculation, mice were intraperitoneally administered the
844 reversal agent atipamezole (Antisedan; ~0.0125 mg/g).
845 Nonperfused mice were euthanized by CO2 asphyxiation and cervical dislocation. Mice
846 that were intracardially perfused at time of death were anesthetized with isoflurane and perfused

847 in a nonrecirculating fashion before cervical dislocation. Fungal burden was assessed by
848 excising organs and homogenizing them in 5 mL 1XPBS, washing the probe in between
849 samples: 30 seconds 10% bleach, 45 seconds 70% EtOH, and 10 seconds sterile H_2O. Ten-fold
850 serial dilutions of organ homogenate were plated on Sabouraud's agar containing 10 mg/ml
851 gentamicin and 100 mg/ml carbenicillin and stored at 30°C for 3 days before counting CFUs.
852 All animal procedures were approved by the University of Utah Institutional Animal Care
853 and Use Committee.
854
855 **Fungal cell size measurements**
856 *C. neoformans* cells harvested from laboratory growth medium or infected mouse lungs
857 were fixed in 2% paraformaldehyde for 20 minutes. To visualize capsule, 4 µl of India ink with 4
858 µl of cell suspension on a microscope slide. At least 10 successive images were taken starting
859 at one edge of the coverslip and moving across to the opposite side, as smaller cells tended to
860 drift to the edge of the coverslips. Total diameter was measured from one edge of the capsule to
861 the other. Cell body diameter was measured from one edge of the cell wall to the other. Capsule
862 thickness was calculated as follows: capsule thickness = (total diameter – cell body diameter) /
863 2. The total number of cells counted for a given experiment is indicated in the figure legends.
864
865 **FACS isolation of fungal cells**
866 Mice were intranasally inoculated with *C. neoformans* KN99-mCherry (see "Mouse
867 infection models"). At 14 dpi, lungs from 3 mice were excised and placed in 15 mL of 1XPBS.
868 The three lungs were homogenized together using a mechanical tissue homogenizer. The
869 homogenate was filtered first through a 70 µM cell strainer and then through a 40 µM cell
870 strainer to prevent downstream clogging of the flow cytometer. Cells were centrifuged at 2195xg
871 for 10 min. The supernatant was discarded and the pellet was resuspended in ~1mL 1XPBS.
872 The suspension was filtered once more through a 70 µM cell strainer and was resuspended at
873 ~$1x10^7$ cells/mL in 1XPBS for FACS (BD FACS Aria). The FACS gating scheme is represented
874 in **Figure 2**.
875
876 **Isolation of polystyrene beads from mouse organs**
877 Mice were intravenously administered (see "Mouse infection models") 10^5 green
878 fluorescent polystyrene beads (Polysciences, Inc. catalog no. 17156-2 and 18241-2), and 3
879 hours later the indicated organs were harvested. Organs were homogenized with a mechanical
880 tissue homogenizer in 5 mL tissue lysis buffer (100 mM Tris-Cl pH 8.0, 200mM NaCl, 5mM

881 EDTA, 0.2% (w/v) SDS), washing the probe in between samples: 15 seconds H_2O, 15 seconds
882 70% EtOH, and 15 seconds fresh H_2O.
883 Beads from each organ were concentrated via differential centrifugation. The
884 homogenates were poured into a fresh 50 mL conical. The homogenization tubes were washed
885 with 30 mL of H_2O and combined with the respective homogenized sample. The samples were
886 filtered through cell strainers (70 μM pore size), after which another 10 mL of H_2O was passed
887 through each strainer. The samples were centrifuged at 4480xg for 40 minutes. The supernatant
888 was aspirated to the 5 mL mark and the samples were transferred to fresh 15 mL tubes
889 containing 2 mL of 100% Percoll (GE Healthcare catalog no. 17-0891-01). Water was added to
890 the 10 mL mark. The tubes were vortexed to mix and allowed to settle for 5 minutes before
891 centrifugation at 1120xg for 45 minutes. The supernatant was aspirated to the 2 mL mark. 10
892 mL of H2O was added to the samples before centrifuging at 4480xg for 20 minutes. The
893 supernatant was aspirated and resuspended in 200-1000 μl 1XPBS for flow cytometry. Entire
894 samples were analyzed to determine the number of beads per organ.
895
896 **Fungal cell staining and flow cytometry analysis**
897 Between 10^5 and 10^6 *C. neoformans* cells harvested from laboratory growth medium or
898 infected mouse lungs were pelleted and fixed in 2% paraformaldehyde for 20 minutes. Fixed
899 cells were pelleted and washed twice with 1XPBS. Cells were then resuspended in 1XPBS and
900 stained with the desired antibodies/lectins/fluorescent dye.
901 To estimate DNA content, cells were stained for 10 minutes (room temperature) in 0.3
902 μg/mL 1XPBS+0.1% triton X-100. Mid-log phase fungal cells grown in YNB medium +/- 80
903 μg/mL benomyl (Agilent catalog no. PST-1245) for 24 hours were used to set 1C and 2C gates.
904 Untreated mid-log phage fungal cells display two DAPI peaks (1C ad 2C), while benomyl
905 prevents cell division and traps cells at 2C.
906 To estimate fungal microbial associated molecular pattern exposure, cells were stained
907 at room temperature with 5 μg/mL fluorescein-conjugated wheat-germ agglutinin (WGA, Vector
908 Laboratories catalog no. FL-1021) for 15 minutes to detect exposed chitin or 50 μg/mL
909 fluorescein-conjugated concanavalin A (ConA, Vector Laboratories catalog no. FL-1001) for 5
910 minutes to detect exposed mannose.
911 To estimate the percentage of cells bound by soluble host factors, we used the following
912 antibodies: α-complement C3 (primary: mAb 11H9, ThermoFisher catalog no. MA1-40046;
913 secondary: Mouse anti-Rat IgG2a, FITC, Thermofisher catalog no. 11-4817-82), α-surfactant
914 protein D (primary: polyclonal, Abcam catalog no. ab203309; secondary: Donkey anti-Rabbit

915 IgG, AlexaFluor 405, Abcam catalog no. ab175651), α-mannose binding lectin A (primary: mAb
916 8G6, Hycult catalog no. HM1035; secondary: Mouse anti-Rat IgG2a, FITC, Thermofisher
917 catalog no. 11-4817-82), α-mannose binding lectin C (primary: mAb 14D12, Abcam catalog no.
918 ab106046; secondary: Mouse anti-Rat IgG2a, FITC, Thermofisher catalog no. 11-4817-82), α-
919 IgM (mAb II/41, FITC, BD Biosciences catalog no. 553437), α-IgA (mAb 11-44-2, FITC,
920 SouthernBiotech catalog no. 1165-02). Cells were stained with primary antibodies (1:50 dilution)
921 for 30 minutes on ice. When a secondary antibody was required, primary antibody labeled cells
922 were pelleted, washed twice with 1XPBS and stained with the secondary antibody (1:50 dilution)
923 for 20 minutes on ice.
924 After staining, cells were pelleted and washed twice with 1mL 1XPBS before being
925 resuspended in 200-400 µl of 1XPBS for flow cytometry.
926
927 **GXM isolation**
928 GXM was isolated as described previously (Wozniak and Levitz, 2009) with slight
929 modifications. *C. neoformans* (KN99) cells were grown in 100 mL for 3 days at 37°C in YNB
930 medium (YNB+2% glucose). Cells were centrifuged for 15 minutes at 12,000xg. The
931 supernatant was filtered (0.45 µM pore size) and 50 mL of supernatant was transferred to a 250
932 mL bottle. ~150 mL of 95% EtOH was added to the samples in 4-5 aliquots, mixing after each
933 addition. Samples were stored at 4°C overnight to precipitate GXM. Samples were centrifuged
934 for 30 minutes at 15,000xg, 4°C. The pellets were resuspended in 0.2M NaCl to a concentration
935 of about 10 mg/mL (~50 mL per 250 mL bottle). Samples were transferred to a clean beaker
936 stirred until samples were completely resuspended. 3 mg hexadecyltrimethylammonium
937 bromide (CTAB) per 1mg precipitate was slowly added with stirring and low heat. Once
938 solubilized, the samples were removed from heat and 250 mL of 0.05% CTAB was slowly
939 added with stirring. The samples were moved to fresh 250 mL bottles and centrifuged at for 2
940 hours at 11,000xg, 4°C. The supernatant was discarded and the pellet was washed in 150 mL
941 of 10% EtOH. The samples were centrifuge for 20 minutes at 15,000xg, room temperature. The
942 supernatant was discarded and the pellets were resuspended in 50 mL of 1M NaCl. The
943 samples were transferred to a clean beaker and stirred until completely resuspended.
944 Approximately 2 volumes of 95% EtOH was added dropwise with stirring to precipitate the GXM
945 while leaving the CTAB in solution. The samples were centrifuged in fresh 250 mL bottles for 20
946 minutes at 11,000xg, room temperature. The supernatant was discarded and the precipitate
947 was dissolved in 2M NaCl. The resulting solution was placed in a snake-skin dialysis cassette
948 with a 3,500 molecular weight cutoff (Thermo Fisher Scientific catalog no. 68035) and dialyzed

949 overnight against 1M NaCl. The samples were subsequently dialyzed against distilled H_2O for
950 14 days at 4°C. The distilled H_2O was changed every 1-2 hours for the first 2 days, and then 4-5
951 times a day for the next 6 days. For the last 2-6 days, the water was changed 2-3 times a day.
952 The dialyzed samples were lyophilized and stored at -80 °C.
953
954 **Cell-type specific depletion in mice**
955 Hepatic and splenic macrophages were depleted from mice using clodronate liposomes.
956 Mice were intravenously administered 200 µl of clodronate liposomes (Liposoma BV catalog no.
957 C-010) or PBS control liposomes (Liposoma BV catalog no. P-010) 48 hours prior to inoculation
958 with *C. neoformans* cells. Macrophage depletion efficiency in the liver and spleen was assessed
959 on the day of inoculation via flow cytometry. Macrophages were identified as CD45+ (anti-
960 CD45-efluor450, eBiosciences catalog no. 48-0451-82) and F4/80+ (anti-F4/80-APC,
961 eBiosciences catalog no. 17-4801-80).
962 Neutrophils were depleted from mice using anti-Ly6G antibodies. Mice were
963 intraperitoneally administered 200 ug of anti-Ly6G (clone 1A8 BioXcell catalog no. BP0075-1)
964 antibodies or PBS control at 24 and 2 hours prior to inoculation with *C. neoformans* cells.
965 Neutrophil depletion efficiency in the blood was assessed on the day of inoculation via flow
966 cytometry. Neutrophils were identified as CD45+ (anti-CD45-efluor450, eBiosciences catalog
967 no. 48-0451-82), CD11b+ (anti-CD11b-APC, eBiosciences catalog no. 17-0112-82), and Ly6G+
968 (anti-Ly6G-FITC, eBiosciences catalog no. 11-5931-82).
969 Platelets were depleted from mice using anti-GPIbα antibodies. Mice were intravenously
970 administered 80 µl of anti-GPIbα antibodies (Emfret catalog no. R300) or PBS control 24 hours
971 prior to inoculation with *C. neoformans* cells. Platelet depletion efficiency was determined by
972 Hemavet 950FS (Drew Scientific Group) analysis of blood collected by cheek bleed 10 minutes
973 prior to anti-GPIbα administration and on the day of inoculation.
974
975 **Liver macrophage isolation and infection**
976 Liver macrophages were isolated from 8- to 10-week-old female C57BL/6NJ mice
977 (Jackson Laboratory) according to established procedures (Li et al., 2014). Isolated liver
978 macrophages were resuspended in complete DMEM (Dulbecco's Modified Eagle's Medium,
979 GenClone catalog no. 25-500) supplemented with 10% fetal bovine serum (FBS, (GenClone
980 catalog no. 25-550) and 100 U/mL Penicillin/Streptomycin and seeded into a T-25 flask at a
981 density of 8-10 × 10^6 cells/flask. Macrophages were allowed to settle and adhere for 4 hours in a
982 mammalian tissue culture incubator (37 °C, 5% CO_2). Non-adherent cells were then removed

983 from the dish by gently washing 3 times with 1XPBS (without divalent cations), leaving adherent
984 macrophages. The media was replaced with 5 mL complete DMEM, and the cells were rested
985 for 4 days. The media was replaced on the day after initial seeding, and then as needed.
986 Fungal infection and association with liver macrophages was assessed using the
987 following procedures. The media was aspirated from rested liver macrophages and the cells
988 were washed once with 1XPBS. Macrophages were lifted from the plate by treating them with
989 1mL Accutase (Corning catalog no. 25-058-CI) for ~5 minutes, tapping the plate to dislodge
990 cells. 1 mL complete DMEM was added to the Accutase-treated cells, which were then
991 centrifuged at 300xg for 5 minutes. Liver macrophages were resuspended cells in 0.5-1 mL
992 complete DMEM and live cells were counted by mixing trypan blue (HyClone catalog no.
993 SV30084.01) with cell suspension at a 1:1 ratio and counting clear cells on a hemocytometer.
994 40,000 live cells/well were seeded into 96-well plates in complete DMEM. The liver
995 macrophages were allowed to settle and adhere overnight.
996 The next day, the inoculum was prepared by resuspending *C. neoformans* cells in 500 µl
997 of 0.01% Direct Yellow 96 (AK Scientific 61725-08-4), vortexing briefly to mix, and incubating for
998 5 minutes on the benchtop. *C. neoformans* cells stained with Direct Yellow 96 were pelleted,
999 washed once with 1 mL 1XPBS, and resuspended at a concentration of $8x10^6$ cells/mL in
1000 serum-free DMEM. The supernatant was aspirated from the macrophages seeded in the 96-well
1001 plates and was replaced with 200 µl of serum-free DMEM. 10 µl of the inoculum ($8x10^4$ cells)
1002 was added to each well, resulting in a multiplicity of infection of 1:1. Macrophages and *C.*
1003 *neoformans* cells were co-cultured for 4 hours in a mammalian tissue culture incubator (37 °C,
1004 5% CO_2). The medium was then aspirated from each well, and the cells were washed three
1005 times with 100 µl of 1XPBS to remove non-macrophage associated fungal cells. The remaining
1006 cells were fixed in 100 µl of 4% paraformaldehyde for 10 min. The paraformaldehyde was then
1007 removed and the cells were washed twice with 100 µl of 1XPBS and stained with100 µl of DAPI
1008 (Sigma Aldrich catalog no. 28718-90-3) working solution (600 nM DAPI; 0.1% Triton X-100; in
1009 1XPBS) for 5 minutes. The DAPI working solution was then removed and cells were washed
1010 twice with 100 µl of 1XPBS. Finally, 100 µl of 1XPBS was added to the wells to prevent
1011 desiccation. Cells were imaged on a Nikon widefield microscope, and the number of
1012 macrophages with associated *C. neoformans* cell(s) were counted (green-fluorescent due to
1013 Direct Yellow 96). Six images were taken per well in the same relative positions and every
1014 imaged macrophage was scored as having a physically associated fungal cell(s) or not,
1015 resulting in 2263-3197 macrophages counted per experimental condition across three
1016 independent replicates.

1017 In order to asses liver macrophage killing of *C. neoformans* cells, liver macrophages
1018 were seeded in 96-well plates and infected with *C. neoformans* cells as described above. The
1019 plates containing *C. neoformans* and macrophages were incubated for 24 or 48 hours. After the
1020 desired time, the supernatant was collected from each well and transferred to a microcentrifuge
1021 tube. 200 µl of sterile distilled water was then added to each well in order to lyse the
1022 macrophages for 40 minutes at 37°C. The contents of each well were then mixed to collect
1023 every *C. neoformans* cell and combined with the respective supernatant now in a
1024 microcentrifuge tube. The wells were rinsed with 200 µl sterile PBS and added to the respective
1025 microcentrifuge tube. Serial dilutions of each of the well contents were plated on YPAD agar
1026 and incubated at 30°C for 2-3 days before counting CFUs. CFUs quantified at each timepoint
1027 were normalized to the CFUs in the inoculum in order to calculate the "% of input". Each
1028 macrophage killing experiment was repeated on three different days with each experimental
1029 condition being performed in duplicate wells.
1030
1031 **Fungal survival in blood**
1032 We collected whole blood from 8- to 10-week-old female C57BL/6NJ mice
1033 (Jackson Laboratory) to assess *C. neoformans* survival in blood. Mice were anesthetized with
1034 isoflurane, and whole blood was collected by cardiac puncture using 28-gauge x 12.7 mm
1035 syringes pre-coated with 0.5M EDTA. Blood was immediately transferred to tubes containing
1036 heparin to achieve a final concentration of 30 units of heparin per mL of blood. 100 µl of blood
1037 was added to individual wells of a 96-well plate. 100 *C. neoformans* cells in 5 ul of 1XPBS were
1038 used to inoculate each well. The plates were incubated in a mammalian tissue culture incubator
1039 (37 °C, 5% CO_2) without shaking. At the indicated timepoint, the well contents were transferred
1040 to fresh microcentrifuge tubes. The wells were washed with 100 ul of 0.05M EDTA, which was
1041 then added to the respective microcentrifuge tube. The entire contents of the microcentrifuge
1042 tubes were plated on YPAD agar and incubated at 30°C for 2-3 days before counting CFUs.
1043 CFUs quantified at each timepoint were normalized to the CFUs in the inoculum in order to
1044 calculate the "% of input". Each experiment was repeated on three different days with each
1045 experimental condition being performed in duplicate wells.
1046
1047 **RNA isolation, sequencing, and analysis**
1048 RNA sequencing data is publicly available at NCBI GEO (Accession number:
1049 GSE152784). *C. neoformans* cells were harvested from laboratory media and from infected
1050 mouse lungs for RNA isolation and sequencing. Three replicates were sequenced for each

1051 sample with replicates being defined as follows. Approximately 10^7 cells were harvested from
1052 the indicated *in vitro* growth condition on three separate days. At least 10^6 *ex vivo* cells were
1053 isolated per sort gate each day (see "FACS isolation of fungal cells"). *Ex vivo* cells were isolated
1054 from the pooled lung homogenate of three mice. *Ex vivo* sample populations were isolated on
1055 two consecutive days and pooled for RNA isolation and sequencing, with the end result being
1056 that each sequenced *ex vivo* replicate represents fungal cells isolated from pools of six mice.
1057 RNA was isolated using phenol-chloroform extraction, followed by Qiagen RNeasy
1058 column-based cleanup. Fungal cells were pelleted, flash frozen in liquid nitrogen, and
1059 lyophilized until completely dry. Lyophilized cells were resuspended in 750 µl of TRIzol
1060 (ThermoFisher Scientific catalog no. 15596026) inside screw-cap microcentrifuge tubes.
1061 Approximately 50 µl of 1-mm and 150 µl of 0.5mm zirconium beads (BioSpec Products catalog
1062 no. 11079110z and 11079105z) were added to each sample and placed in a Biospec Products
1063 mini bead beater to lyse (12 x 2 min beating pulses, using sample blocks stored at -20 °C to
1064 prevent overheating). 150 µl of chloroform was added to the lysed samples and incubated for 2-
1065 3min at room temperature. Samples were centrifuged for 15 minutes at 12,000 x *g*, 4°C. The
1066 aqueous phase was transferred to a fresh tube and combined with 5-10 µg RNase-free
1067 glycogen as a carrier. 0.375 mL of isopropanol was added to each sample before incubating at
1068 least ~20 minutes on ice. The samples were centrifuged for 15 minutes at 12,000 x *g*, 4°C. The
1069 supernatant was discarded, and the isopropanol was removed by pipetting. The samples were
1070 then briefly air-dried before resuspension in 350 µl of RLT buffer (Qiagen RNeasy) and 350 µl
1071 70% EtOH. At this junction, samples were run through Qiagen's RNAeasy kit (Qiagen catalog
1072 no. 74104) with on-column DNase treatment.
1073 cDNA libraries were generated with the NEBNext Ultra II Directional RNA Library Prep
1074 with rRNA Depletion Kit (New England BioLabs catalog no. E7760) by the High Throughput
1075 Genomics Core at the University of Utah. Sample libraries were sequenced on the Illumina
1076 NovaSeq 6000. One set of samples (primarily the *ex vivo* small, medium, and large cells) were
1077 stored by the High Throughput Genomics Core at -80°C for six months prior to library
1078 construction and showed more degradation products than replicates stored at -80°C for one
1079 month. We therefore limited our analysis and interpretation of the data from these samples.
1080 The *Cryptococcus neoformans* var. grubii H99 genome and gene feature files were
1081 downloaded from Ensembl Fungi release 46 and the reference database was created using
1082 STAR version 2.7.2c with splice junctions optimized for 150 base pair reads (Dobin et al., 2013).
1083 Optical duplicates were removed from the paired end FASTQ files using clumpify v38.34 and
1084 reads were trimmed of adapters using cutadapt 1.16 (Martin, 2011). The trimmed reads were

1085 aligned to the reference database using STAR in two pass mode to output a BAM file sorted by
1086 coordinates. Mapped reads were assigned to annotated genes in the gene feature file using
1087 featureCounts version 1.6.3 (Liao et al., 2013). The output files from cutadapt, FastQC, Picard
1088 CollectRnaSeqMetrics, STAR and featureCounts were summarized using MultiQC to check for
1089 any sample outliers (Ewels et al., 2016). Differentially expressed genes were identified using a
1090 5% false discovery rate with DESeq2 version 1.24.0 (Love et al., 2014). Differentially expressed
1091 genes were run through FungiDB Gene Ontology (GO) Enrichment analysis, selecting for
1092 "biological process" with a p-value cutoff of 0.05 (Basenko et al., 2018; Stajich et al., 2012).
1093 Venn Diagrams were made with software from the Van de Peer group at Ghent University
1094 (http://bioinformatics.psb.ugent.be/webtools/Venn/).
1095
1096 **Lung pH measurements**
1097 To measure lung tissue pH, mouse lungs were excised and immediately pierced with a
1098 micro pH electrode (Orion (ThermoFisher Scientific) catalog no. 9863BN). The electrode was
1099 completely embedded in the lung tissue before taking pH readings. Two readings were taken
1100 per mouse. One reading was taken from the left lobe of the lungs and a second reading was
1101 taken from one of the right lobes. These two readings were averaged to estimate lung pH for a
1102 given mouse.
1103
1104 **Construction of the KN99:*pho4*Δ strains**
1105 The KN99:*pho4*Δ (*CNAG_06751*Δ) strains were constructed via homologous
1106 recombination-based replacement of the *pho4* genomic sequence with a nourseothicin
1107 resistance marker. The KN99:*pho4*Δ #1 strain was obtained from the KN99 gene deletion library
1108 (Fungal Genetics Stock Center, 2015 Madhani plates). The KN99:*pho4*Δ #2 strain was
1109 generated by PCR amplification of the nourseothicin resistance marker and ~1,000 base pair
1110 flanking regions from the KN99:*pho4*Δ #1 strain (primers used to amplify the knock-out
1111 construct: Forward: 5' AAAACGGCTGAAGGCTCGTTCT3', Reverse:
1112 CTTCTGCAAGGTGAAGTTCACG). The resulting pho4 knock-out cassette was used to
1113 transform wild-type KN99 cells via biolistic transformation as described previously (Davidson et
1114 al., 2000). Putative transformants were PCR-verified by confirming the absence of the *pho4*
1115 open reading frame (Primers to verify the absence of the open reading frame: Forward:
1116 5'CCATCTCAGATACCAACTCGCC', Reverse: 5'CAATTTGCTGAGAGCCATAGGC3') and the
1117 integration of the knock-out construct at the correct site (Primers to verify the correct 5'
1118 integration site: Forward: 5'AGAGCTATATGGTATGACGAAC3', Reverse:

1119 5'TGTGCTGATCATCCGATGCCAC3' and the correct 3' integration site: Forward
1120 5'TGTGGAGGATGGTGGGGAATAG3', Reverse: 5'GGACGTGAGCCAATAAGTTCCT3'.
1121

1122 **Statistics**

1123 All statistical analyses, with the exception of RNA sequencing analysis, were performed
1124 with GraphPad Prism 8 software. Hypothesis-driven experimental comparisons were analyzed
1125 by unpaired t-test or one-way ANOVA and uncorrected Fisher's LSD if the data held a Gaussian
1126 distribution and a Mann-Whitney U-test if the data were not Gaussian. *In vitro* experiments were
1127 replicated three times unless otherwise stated. *In vivo* (murine infection) experiments were
1128 replicated twice unless otherwise stated.
1129

1130 **REFERENCES:**

1131 Alanio, A., Vernel-Pauillac, F., Sturny-Leclère, A., and Dromer, F. (2015). *Cryptococcus*
1132 *neoformans* Host Adaptation: Toward Biological Evidence of Dormancy. mBio *6*, e02580-
1133 02514.
1134 Albuquerque, P., Nicola, A.M., Nieves, E., Paes, H.C., Williamson, P.R., Silva-Pereira, I., and
1135 Casadevall, A. (2014). Quorum sensing-mediated, cell density-dependent regulation of growth
1136 and virulence in *Cryptococcus neoformans*. mBio *5*, e00986-00913.
1137 Basenko, E.Y., Pulman, J.A., Shanmugasundram, A., Harb, O.S., Crouch, K., Starns, D.,
1138 Warrenfeltz, S., Aurrecoechea, C., Stoeckert, C.J., Jr., Kissinger, J.C.*, et al.* (2018). FungiDB: an
1139 integrated bioinformatic resource for fungi and oomycetes. J Fungi *4*, 39.
1140 Bojarczuk, A., Miller, K.A., Hotham, R., Lewis, A., Ogryzko, N.V., Kamuyango, A.A., Frost,
1141 H., Gibson, R.H., Stillman, E., May, R.C.*, et al.* (2016). *Cryptococcus neoformans* intracellular
1142 proliferation and capsule size determines early macrophage control of infection. Sci Rep *6*,
1143 21489.
1144 Broadley, Steven P., Plaumann, A., Coletti, R., Lehmann, C., Wanisch, A., Seidlmeier, A., Esser,
1145 K., Luo, S., Rämer, Patrick C., Massberg, S.*, et al.* (2016). Dual-track clearance of circulating
1146 bacteria balances rapid restoration of blood sterility with induction of adaptive immunity. Cell
1147 Host Microbe *20*, 36-48.
1148 Casadevall, A., Coelho, C., Cordero, R.J.B., Dragotakes, Q., Jung, E., Vij, R., and Wear, M.P.
1149 (2019). The capsule of *Cryptococcus neoformans*. Virulence *10*, 822-831.
1150 Charlier, C., Chrétien, F., Baudrimont, M., Mordelet, E., Lortholary, O., and Dromer, F. (2005).
1151 Capsule structure changes associated with *Cryptococcus neoformans* crossing of the blood-brain
1152 barrier. Am J Pathol *166*, 421-432.
1153 Crabtree, J.N., Okagaki, L.H., Wiesner, D.L., Strain, A.K., Nielsen, J.N., and Nielsen, K. (2012).
1154 Titan cell production enhances the virulence of *Cryptococcus neoformans*. Infect Immun *80*,
1155 3776-3785.
1156 Dambuza, I.M., Drake, T., Chapuis, A., Zhou, X., Correia, J., Taylor-Smith, L., LeGrave, N.,
1157 Rasmussen, T., Fisher, M.C., Bicanic, T.*, et al.* (2018). The *Cryptococcus neoformans* titan cell
1158 is an inducible and regulated morphotype underlying pathogenesis. PLoS Pathog *14*, e1006978.
1159 Dan, J.M., Kelly, R.M., Lee, C.K., and Levitz, S.M. (2008). Role of the mannose receptor in a
1160 murine model of *Cryptococcus neoformans* infection. Infect Immun *76*, 2362-2367.

1161 Davidson, R.C., Cruz, M.C., Sia, R.A.L., Allen, B., Alspaugh, J.A., and Heitman, J. (2000).
1162 Gene disruption by biolistic transformation in serotype D strains of Cryptococcus neoformans.
1163 Fungal Genetics and Biology *29*, 38-48.
1164 Davis, K.M. (2018). All *Yersinia* are not created equal: phenotypic adaptation to distinct niches
1165 within mammalian tissues. Front Cell Infect Microbiol *8*, 261-261.
1166 Davis, K.M., Mohammadi, S., and Isberg, R.R. (2015). Community behavior and spatial
1167 regulation within a bacterial microcolony in deep tissue sites serves to protect against host attack.
1168 Cell Host Microbe *17*, 21-31.
1169 Denham, S.T., and Brown, J.C.S. (2018). Mechanisms of pulmonary escape and dissemination
1170 by *Cryptococcus neoformans*. J Fungi *4*, 25.
1171 Denham, S.T., Verma, S., Reynolds, R.C., Worne, C.L., Daugherty, J.M., Lane, T.E., and
1172 Brown, J.C.S. (2017). Regulated release of cryptococcal polysaccharide drives virulence and
1173 suppresses immune infiltration into the central nervous system. Infect Immun.
1174 Dobin, A., Davis, C.A., Schlesinger, F., Drenkow, J., Zaleski, C., Jha, S., Batut, P., Chaisson,
1175 M., and Gingeras, T.R. (2013). STAR: ultrafast universal RNA-seq aligner. Bioinformatics *29*,
1176 15-21.
1177 Eisen, D.P., Dean, M.M., O'Sullivan, M.V.N., Heatley, S., and Minchinton, R.M. (2008).
1178 Mannose-binding lectin deficiency does not appear to predispose to cryptococcosis in non-
1179 immunocompromised patients. Med Mycol *46*, 371-375.
1180 Emmons, C.W. (1955). Saprophytic sources of *Cryptococcus neoformans* associated with the
1181 pigeon (COLUMBA LIVIA)1. Am J Epidemiol *62*, 227-232.
1182 Ewels, P., Magnusson, M., Lundin, S., and Käller, M. (2016). MultiQC: summarize analysis
1183 results for multiple tools and samples in a single report. Bioinformatics *32*, 3047-3048.
1184 Fang, W., Fa, Z., and Liao, W. (2015). Epidemiology of *Cryptococcus* and cryptococcosis in
1185 China. Fungal Genet Biol *78*, 7-15.
1186 Farhi, F., Bulmer, G.S., and Tacker, J.R. (1970). *Cryptococcus neoformans* IV. The not-so-
1187 encapsulated yeast. Infect Immun *1*, 526-531.
1188 Feldmesser, M., Kress, Y., and Casadevall, A. (2001). Dynamic changes in the morphology of
1189 *Cryptococcus neoformans* during murine pulmonary infection. Microbiol *147*, 2355-2365.
1190 Fernandes, K.E., Brockway, A., Haverkamp, M., Cuomo, C.A., van Ogtrop, F., Perfect, J.R., and
1191 Carter, D.A. (2018). Phenotypic variability correlates with clinical outcome in *Cryptococcus*
1192 isolates obtained from Botswanan HIV/AIDS patients. mBio *9*, e02016-02018.
1193 Gabow, P.A., Kaehny, W.D., and Kelleher, S.P. (1982). The spectrum of rhabdomyolysis.
1194 Medicine (Baltimore) *61*, 141-152.
1195 Gerstein, A.C., Fu, M.S., Mukaremera, L., Li, Z., Ormerod, K.L., Fraser, J.A., Berman, J., and
1196 Nielsen, K. (2015). Polyploid Titan Cells Produce Haploid and Aneuploid Progeny To Promote
1197 Stress Adaptation. mBio *6*.
1198 Geunes-Boyer, S., Beers, M.F., Perfect, J.R., Heitman, J., and Wright, J.R. (2012). Surfactant
1199 protein D facilitates *Cryptococcus neoformans* infection. Infect Immun *80*, 2444.
1200 Goldman, D.L., Khine, H., Abadi, J., Lindenberg, D.J., Pirofski, L.-a., Niang, R., and
1201 Casadevall, A. (2001). Serologic evidence for *Cryptococcus neoformans* infection in early
1202 childhood. Pediatrics *107*, e66-e66.
1203 Himmelreich, U., Allen, C., Dowd, S., Malik, R., Shehan, B.P., Mountford, C., and Sorrell, T.C.
1204 (2003). Identification of metabolites of importance in the pathogenesis of pulmonary
1205 cryptococcoma using nuclear magnetic resonance spectroscopy. Microb Infect *5*, 285-290.

1206 Homer, C.M., Summers, D.K., Goranov, A.I., Clarke, S.C., Wiesner, D.L., Diedrich, J.K.,
1207 Moresco, J.J., Toffaletti, D., Upadhya, R., Caradonna, I.*, et al.* (2016). Intracellular action of a
1208 secreted peptide required for fungal virulence. Cell Host Microbe *19*, 849-864.
1209 Hommel, B., Mukaremera, L., Cordero, R.J.B., Coelho, C., Desjardins, C.A., Sturny-Leclère, A.,
1210 Janbon, G., Perfect, J.R., Fraser, J.A., Casadevall, A.*, et al.* (2018). Titan cells formation in
1211 *Cryptococcus neoformans* is finely tuned by environmental conditions and modulated by positive
1212 and negative genetic regulators. PLoS Pathog *14*, e1006982.
1213 Ikeh, M.A.C., Kastora, S.L., Day, A.M., Herrero-de-Dios, C.M., Tarrant, E., Waldron, K.J.,
1214 Banks, A.P., Bain, J.M., Lydall, D., Veal, E.A.*, et al.* (2016). Pho4 mediates phosphate
1215 acquisition in *Candida albicans* and is vital for stress resistance and metal homeostasis. Mol Biol
1216 Cell *27*, 2784-2801.
1217 Köhler, J.R., Acosta-Zaldívar, M., and Qi, W. (2020). Phosphate in virulence of *Candida*
1218 *albicans* and *Candida glabrata*. J Fungi *6*, 40.
1219 Kowalski, C.H., Kerkaert, J.D., Liu, K.-W., Bond, M.C., Hartmann, R., Nadell, C.D., Stajich,
1220 J.E., and Cramer, R.A. (2019). Fungal biofilm morphology impacts hypoxia fitness and disease
1221 progression. Nat Microbiol *4*, 2430-2441.
1222 Kretschmer, M., Reiner, E., Hu, G., Tam, N., Oliveira, D.L., Caza, M., Yeon, J.H., Kim, J.,
1223 Kastrup, C.J., Jung, W.H.*, et al.* (2014). Defects in phosphate acquisition and storage influence
1224 virulence of *Cryptococcus neoformans*. Infect Immun *82*, 2697-2712.
1225 Lazéra, M.S., Pires, F.D.A., Camillo-Coura, L., Nishikawa, M.M., Bezerra, C.C.F., Trilles, L.,
1226 and Wanke, B. (1996). Natural habitat of *Cryptococcus neoformans var. neoformans* in decaying
1227 wood forming hollows in living trees. J M Vet Mycol *34*, 127-131.
1228 Lee, H., Chang, Y.C., Nardone, G., and Kwon-Chung, K.J. (2007). TUP1 disruption in
1229 *Cryptococcus neoformans* uncovers a peptide-mediated density-dependent growth phenomenon
1230 that mimics quorum sensing. Mol Microbiol *64*, 591-601.
1231 Lev, S., and Djordjevic, J.T. (2018). Why is a functional PHO pathway required by fungal
1232 pathogens to disseminate within a phosphate-rich host: a paradox explained by alkaline pH-
1233 simulated nutrient deprivation and expanded PHO pathway function. PLoS Pathog *14*, e1007021.
1234 Lev, S., Kaufman-Francis, K., Desmarini, D., Juillard, P.G., Li, C., Stifter, S.A., Feng, C.G.,
1235 Sorrell, T.C., Grau, G.E.R., Bahn, Y.-S.*, et al.* (2017). Pho4 is essential for dissemination of
1236 *Cryptococcus neoformans* to the host brain by promoting phosphate uptake and growth at
1237 alkaline pH. mSphere *2*, e00381-00316.
1238 Li, P.-z., Li, J.-z., Li, M., Gong, J.-p., and He, K. (2014). An efficient method to isolate and
1239 culture mouse Kupffer cells. Immunol Lett *158*, 52-56.
1240 Li, Z., and Nielsen, K. (2017). Morphology changes in human fungal pathogens upon interaction
1241 with the host. J Fungi *3*, 66.
1242 Liao, Y., Smyth, G.K., and Shi, W. (2013). featureCounts: an efficient general purpose program
1243 for assigning sequence reads to genomic features. Bioinformatics *30*, 923-930.
1244 Lim, J., Coates, C.J., Seoane, P.I., Garelnabi, M., Taylor-Smith, L.M., Monteith, P., Macleod,
1245 C.L., Escaron, C.J., Brown, G.D., Hall, R.A.*, et al.* (2018). Characterizing the mechanisms of
1246 nonopsonic uptake of Cryptococci by macrophages. J Immunol *200*, 3539-3546.
1247 Lin, Y.-Y., Shiau, S., and Fang, C.-T. (2015). Risk factors for invasive *Cryptococcus neoformans*
1248 diseases: a case-control study. PloS One *10*, e0119090-e0119090.
1249 Liu, N.-N., Uppuluri, P., Broggi, A., Besold, A., Ryman, K., Kambara, H., Solis, N., Lorenz, V.,
1250 Qi, W., Acosta-Zaldívar, M.*, et al.* (2018). Intersection of phosphate transport, oxidative stress
1251 and TOR signalling in *Candida albicans* virulence. PLoS Pathog *14*, e1007076.

1252 Love, M.I., Huber, W., and Anders, S. (2014). Moderated estimation of fold change and
1253 dispersion for RNA-seq data with DESeq2. Genome Biol *15*, 550.
1254 Macpherson, A.J., Heikenwalder, M., and Ganal-Vonarburg, S.C. (2016). The liver at the nexus
1255 of host-microbial interactions. Cell Host Microbe *20*, 561-571.
1256 Martin, M. (2011). Cutadapt removes adapter sequences from high-throughput sequencing reads.
1257 EMBnet *17*, 10-12.
1258 Maziarz, E.K., and Perfect, J.R. (2016). Cryptococcosis. Infect Dis Clin North Am *30*, 179-206.
1259 Mukaremera, L., McDonald, T.R., Nielsen, J.N., Molenaar, C.J., Akampurira, A., Schutz, C.,
1260 Taseera, K., Muzoora, C., Meintjes, G., Meya, D.B.*, et al.* (2019). The mouse inhalation model
1261 of *Cryptococcus neoformans* infection recapitulates strain virulence in humans and shows that
1262 closely related strains can possess differential virulence. Infect Immun *87*, e00046-00019.
1263 Ngamskulrungroj, P., Chang, Y., Sionov, E., and Kwon-Chung, K.J. (2012a). The Primary
1264 Target Organ of Cryptococcus gattii Is Different from That of Cryptococcus neoformans in a
1265 Murine Model. *3*, e00103-00112.
1266 Ngamskulrungroj, P., Chang, Y., Sionov, E., and Kwon-Chung, K.J. (2012b). The primary target
1267 organ of *Cryptococcus gattii* is different from that of *Cryptococcus neoformans* in a murine
1268 model. mBio *3*, e00103-00112.
1269 O'Meara, T.R., and Alspaugh, J.A. (2012). The *Cryptococcus neoformans* capsule: a sword and a
1270 shield. Clin Microbiol Rev *25*, 387-408.
1271 Okagaki, L.H., and Nielsen, K. (2012a). Titan Cells Confer Protection from Phagocytosis in
1272 *Cryptococcus neoformans* Infections. *11*, 820-826.
1273 Okagaki, L.H., and Nielsen, K. (2012b). Titan cells confer protection from phagocytosis in
1274 *Cryptococcus neoformans* infections. Eukaryot Cell *11*, 820-826.
1275 Okagaki, L.H., Strain, A.K., Nielsen, J.N., Charlier, C., Baltes, N.J., Chrétien, F., Heitman, J.,
1276 Dromer, F., and Nielsen, K. (2010). Cryptococcal cell morphology affects host cell interactions
1277 and pathogenicity. PLoS Pathog *6*, e1000953.
1278 Okagaki, L.H., Wang, Y., Ballou, E.R., O'Meara, T.R., Bahn, Y.-S., Alspaugh, J.A., Xue, C., and
1279 Nielsen, K. (2011). Cryptococcal titan cell formation is regulated by G-protein signaling in
1280 response to multiple stimuli. Eukaryot Cell *10*, 1306-1316.
1281 Panepinto, J.C., Komperda, K.W., Hacham, M., Shin, S., Liu, X., and Williamson, P.R. (2007).
1282 Binding of serum mannan binding lectin to a cell integrity-defective *Cryptococcus neoformans*
1283 ccr4Delta mutant. Infect Immun *75*, 4769-4779.
1284 Pearson, A.M., Rich, A., and Krieger, M. (1993). Polynucleotide binding to macrophage
1285 scavenger receptors depends on the formation of base-quartet-stabilized four-stranded helices. J
1286 Biol Chem *268*, 3546-3554.
1287 Rajasingham, R., Smith, R.M., Park, B.J., Jarvis, J.N., Govender, N.P., Chiller, T.M., Denning,
1288 D.W., Loyse, A., and Boulware, D.R. (2017). Global burden of disease of HIV-associated
1289 cryptococcal meningitis: an updated analysis. Lancet Infect Dis *17*, 873-881.
1290 Rivera, J., Feldmesser, M., Cammer, M., and Casadevall, A. (1998). Organ-dependent variation
1291 of capsule thickness in *Cryptococcus neoformans* during experimental murine infection. Infect
1292 Immun *66*, 5027-5030.
1293 Sabiiti, W., May, R.C., and Pursall, E.R. (2012). Experimental models of cryptococcosis. Int J
1294 Microbiol *2012*, 626745-626745.
1295 Sahly, H., Ofek, I., Podschun, R., Brade, H., He, Y., Ullmann, U., and Crouch, E. (2002).
1296 Surfactant protein D binds selectively to lipopolysaccharides containing mannose-rich O-
1297 antigens. J Immunol *169*, 3267.

1298 San Juan, B.P., Garcia-Leon, M.J., Rangel, L., Goetz, J.G., and Chaffer, C.L. (2019). The
1299 complexities of metastasis. Cancers (Basel) *11*, 1575.
1300 Selmecki, A.M., Maruvka, Y.E., Richmond, P.A., Guillet, M., Shoresh, N., Sorenson, A.L., De,
1301 S., Kishony, R., Michor, F., Dowell, R.*, et al.* (2015). Polyploidy can drive rapid adaptation in
1302 yeast. Nature *519*, 349-352.
1303 Stajich, J.E., Harris, T., Brunk, B.P., Brestelli, J., Fischer, S., Harb, O.S., Kissinger, J.C., Li, W.,
1304 Nayak, V., Pinney, D.F.*, et al.* (2012). FungiDB: an integrated functional genomics database for
1305 fungi. Nucleic Acids Res *40*, D675-D681.
1306 Sun, D., Sun, P., Li, H., Zhang, M., Liu, G., Strickland, A.B., Chen, Y., Fu, Y., Xu, J., Yosri, M.*,*
1307 *et al.* (2019). Fungal dissemination is limited by liver macrophage filtration of the blood. Nat
1308 Commun *10*, 4566.
1309 Sun, D., Zhang, M., Liu, G., Wu, H., Li, C., Zhou, H., Zhang, X., and Shi, M. (2016).
1310 Intravascular clearance of disseminating *Cryptococcus neoformans* in the brain can be improved
1311 by enhancing neutrophil recruitment in mice. Eur J Immunol *46*, 1704-1714.
1312 Todd, R.T., Braverman, A.L., and Selmecki, A. (2018). Flow Cytometry Analysis of Fungal
1313 Ploidy. Curr Protoc Microbiol *50*, e58-e58.
1314 Trevijano-Contador, N., de Oliveira, H.C., García-Rodas, R., Rossi, S.A., Llorente, I., Zaballos,
1315 Á., Janbon, G., Ariño, J., and Zaragoza, Ó. (2018). *Cryptococcus neoformans* can form titan-like
1316 cells in vitro in response to multiple signals. PLoS Pathog *14*, e1007007.
1317 Walsh, N.M., Botts, M.R., McDermott, A.J., Ortiz, S.C., Wüthrich, M., Klein, B., and Hull, C.M.
1318 (2019). Infectious particle identity determines dissemination and disease outcome for the inhaled
1319 human fungal pathogen *Cryptococcus*. PLoS Pathog *15*, e1007777-e1007777.
1320 Wang, L., and Lin, X. (2015). The morphotype heterogeneity in *Cryptococcus neoformans*. Curr
1321 Opin Microbiol *26*, 60-64.
1322 Weigel, W.A., and Dersch, P. (2018). Phenotypic heterogeneity: a bacterial virulence strategy.
1323 Microb Infect *20*, 570-577.
1324 Wozniak, K.L., and Levitz, S.M. (2009). Isolation and purification of antigenic components of
1325 *Cryptococcus*. Methods Mol Biol *470*, 71-83.
1326 Wright, L., Bubb, W., Davidson, J., Santangelo, R., Krockenberger, M., Himmelreich, U., and
1327 Sorrell, T. (2002). Metabolites released by *Cryptococcus neoformans var. neoformans* and *var.*
1328 *gattii* differentially affect human neutrophil function. Microb Infect *4*, 1427-1438.
1329 Xie, S., Sao, R., Braun, A., and Bottone, E.J. (2012). Difference in *Cryptococcus neoformans*
1330 cellular and capsule size in sequential pulmonary and meningeal infection: a postmortem study.
1331 Diagn Microbiol Infect Dis *73*, 49-52.
1332 Zaragoza, O. (2011). Multiple disguises for the same party: the concepts of morphogenesis and
1333 phenotypic variations in *Cryptococcus neoformans*. Front Microbiol *2*, 181-181.
1334 Zaragoza, O., García-Rodas, R., Nosanchuk, J.D., Cuenca-Estrella, M., Rodríguez-Tudela, J.L.,
1335 and Casadevall, A. (2010). Fungal cell gigantism during mammalian infection. PLoS Pathog *6*,
1336 e1000945.
1337 Zhang, M., Sun, D., Liu, G., Wu, H., Zhou, H., and Shi, M. (2016). Real-time *in vivo* imaging
1338 reveals the ability of neutrophils to remove *Cryptococcus neoformans* directly from the brain
1339 vasculature. J Leukoc Biol *99*, 467-473.
1340 Zhao, Y., Wang, Y., Upadhyay, S., Xue, C., and Lin, X. (2020). Activation of meiotic genes
1341 mediates ploidy reduction during cryptococcal infection. Curr Biol.
1342 Zhou, X., and Ballou, E.R. (2018). The *Cryptococcus neoformans* titan cell: from *in vivo*
1343 phenomenon to *in vitro* model. Curr Clin Microbiol Rep *5*, 252-260.

1344 Zhou, X., Zafar, H., Sephton-Clark, P., Mohamed, S.H., Chapuis, A., Makarova, M.,
1345 MacCallum, D.M., Drummond, R.A., Dambuza, I.M., and Ballou, E.R. (2020). Host
1346 environmental conditions induce small fungal cell size and alter population heterogeneity in
1347 *Cryptococcus neoformans*. bioRxiv, 2020.2001.2003.894709.
1348

Figure 1

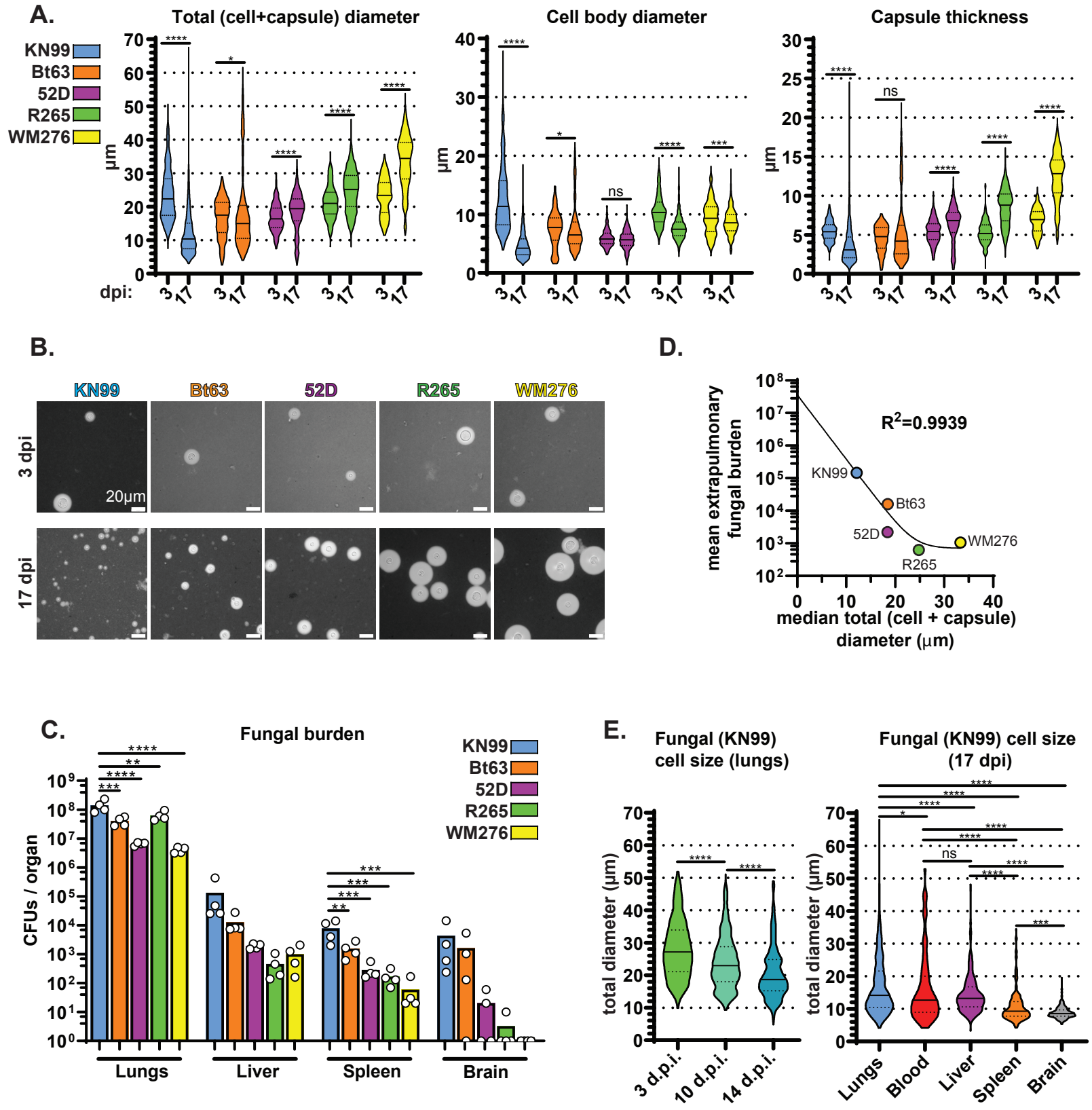
A.
Total (cell+capsule) diameter
Cell body diameter
Capsule thickness
KN99
Bt63
52D
R265
WM276
µm
dpi:
3
17
ns
B.
KN99
Bt63
52D
R265
WM276
3 dpi
17 dpi
20µm
D.
mean extrapulmonary fungal burden
R²=0.9939
KN99
Bt63
52D
R265
WM276
median total (cell + capsule) diameter (µm)
C.
Fungal burden
CFUs / organ
Lungs
Liver
Spleen
Brain
E.
Fungal (KN99) cell size (lungs)
Fungal (KN99) cell size (17 dpi)
total diameter (µm)
3 d.p.i.
10 d.p.i.
14 d.p.i.
Lungs
Blood
Liver
Spleen
Brain

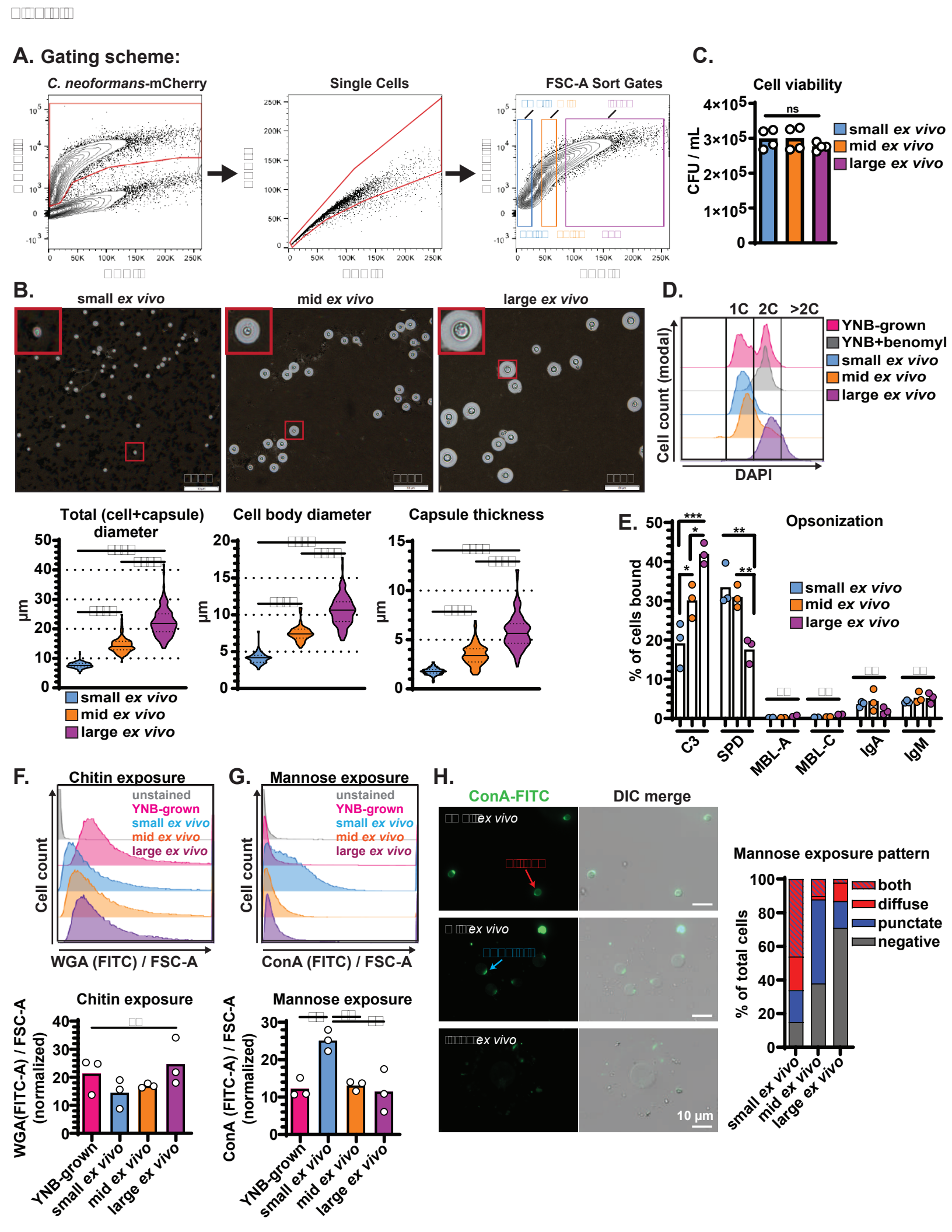
A. Gating scheme:
C. neoformans-mCherry
Single Cells
FSC-A Sort Gates
C.
Cell viability
ns
CFU / mL
small ex vivo
mid ex vivo
large ex vivo
B.
small ex vivo
mid ex vivo
large ex vivo
D.
1C 2C >2C
YNB-grown
YNB+benomyl
small ex vivo
mid ex vivo
large ex vivo
Cell count (modal)
DAPI
Total (cell+capsule) diameter
Cell body diameter
Capsule thickness
µm
small ex vivo
mid ex vivo
large ex vivo
E.
Opsonization
% of cells bound
small ex vivo
mid ex vivo
large ex vivo
C3
SPD
MBL-A
MBL-C
IgA
IgM
F.
Chitin exposure
unstained
YNB-grown
small ex vivo
mid ex vivo
large ex vivo
Cell count
WGA (FITC) / FSC-A
G.
Mannose exposure
unstained
YNB-grown
small ex vivo
mid ex vivo
large ex vivo
Cell count
ConA (FITC) / FSC-A
Chitin exposure
WGA(FITC-A) / FSC-A (normalized)
YNB-grown
small ex vivo
mid ex vivo
large ex vivo
Mannose exposure
ConA (FITC-A) / FSC-A (normalized)
YNB-grown
small ex vivo
mid ex vivo
large ex vivo
H.
ConA-FITC
DIC merge
ex vivo
ex vivo
ex vivo
10 µm
Mannose exposure pattern
% of total cells
both
diffuse
punctate
negative
small ex vivo
mid ex vivo
large ex vivo

Figure 3

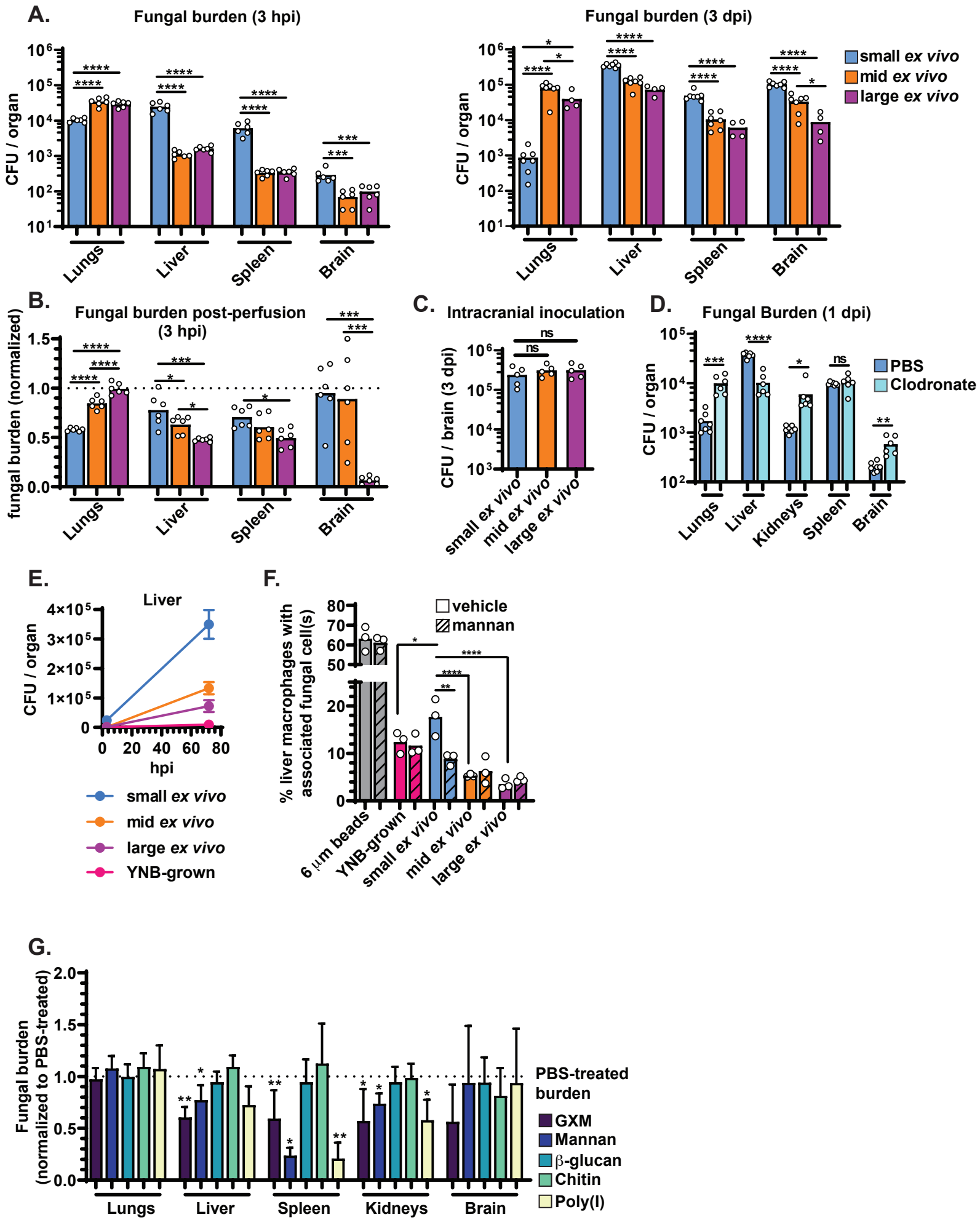
A.
Fungal burden (3 hpi)
CFU / organ
Lungs
Liver
Spleen
Brain
Fungal burden (3 dpi)
small ex vivo
mid ex vivo
large ex vivo
B.
Fungal burden post-perfusion (3 hpi)
fungal burden (normalized)
C.
Intracranial inoculation
CFU / brain (3 dpi)
small ex vivo
mid ex vivo
large ex vivo
D.
Fungal Burden (1 dpi)
PBS
Clodronate
Kidneys
E.
Liver
hpi
small ex vivo
mid ex vivo
large ex vivo
YNB-grown
F.
vehicle
mannan
% liver macrophages with associated fungal cell(s)
6 μm beads
YNB-grown
small ex vivo
mid ex vivo
large ex vivo
G.
Fungal burden (normalized to PBS-treated)
PBS-treated burden
GXM
Mannan
β-glucan
Chitin
Poly(I)
Lungs
Liver
Spleen
Kidneys
Brain

Figure 4

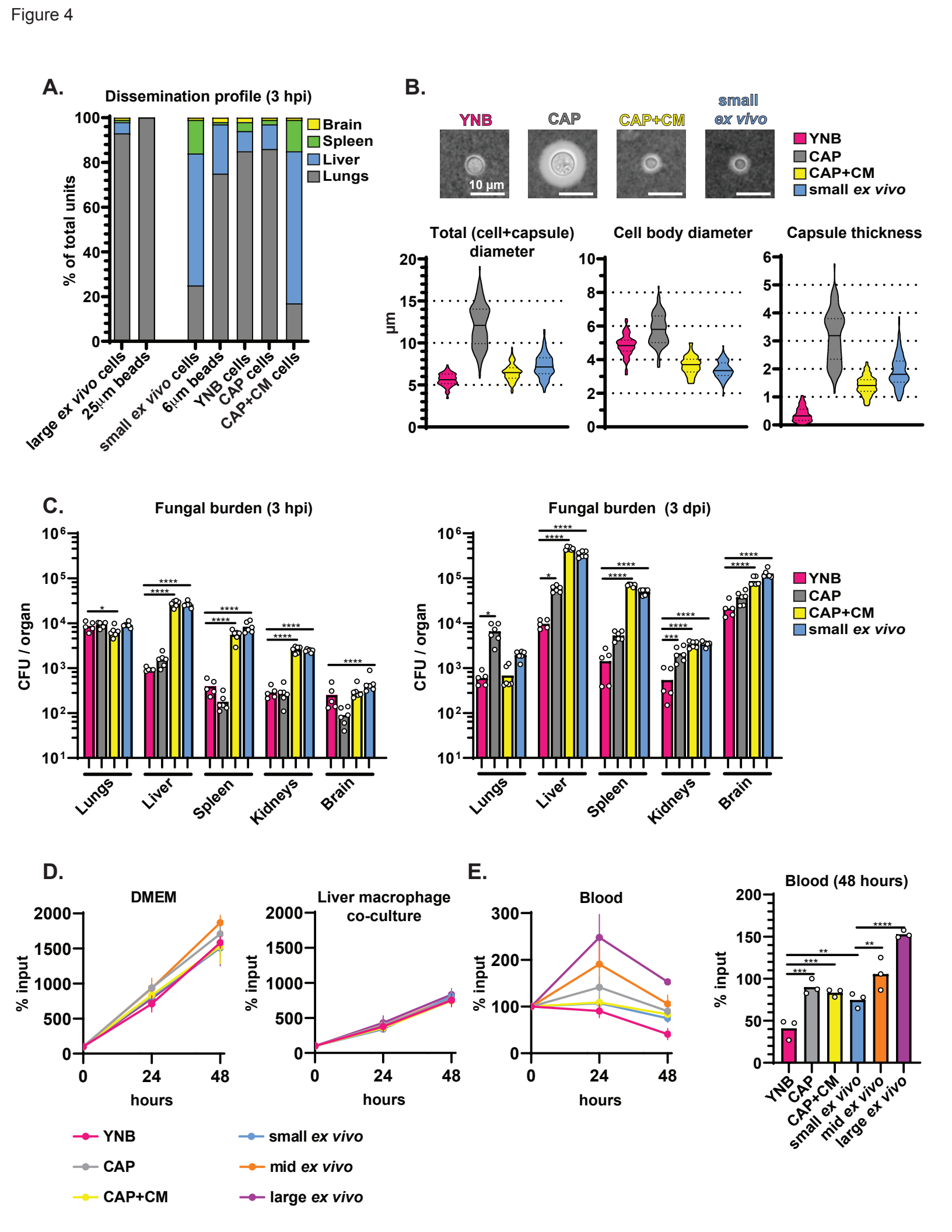
A.
Dissemination profile (3 hpi)
% of total units
Brain
Spleen
Liver
Lungs
large ex vivo cells
25µm beads
small ex vivo cells
6µm beads
YNB cells
CAP cells
CAP+CM cells
B.
YNB
CAP
CAP+CM
small ex vivo
10 µm
Total (cell+capsule) diameter
Cell body diameter
Capsule thickness
µm
C.
Fungal burden (3 hpi)
Fungal burden (3 dpi)
CFU / organ
Lungs
Liver
Spleen
Kidneys
Brain
D.
DMEM
Liver macrophage co-culture
% input
hours
E.
Blood
Blood (48 hours)
YNB
CAP
CAP+CM
small ex vivo
mid ex vivo
large ex vivo

Figure 5

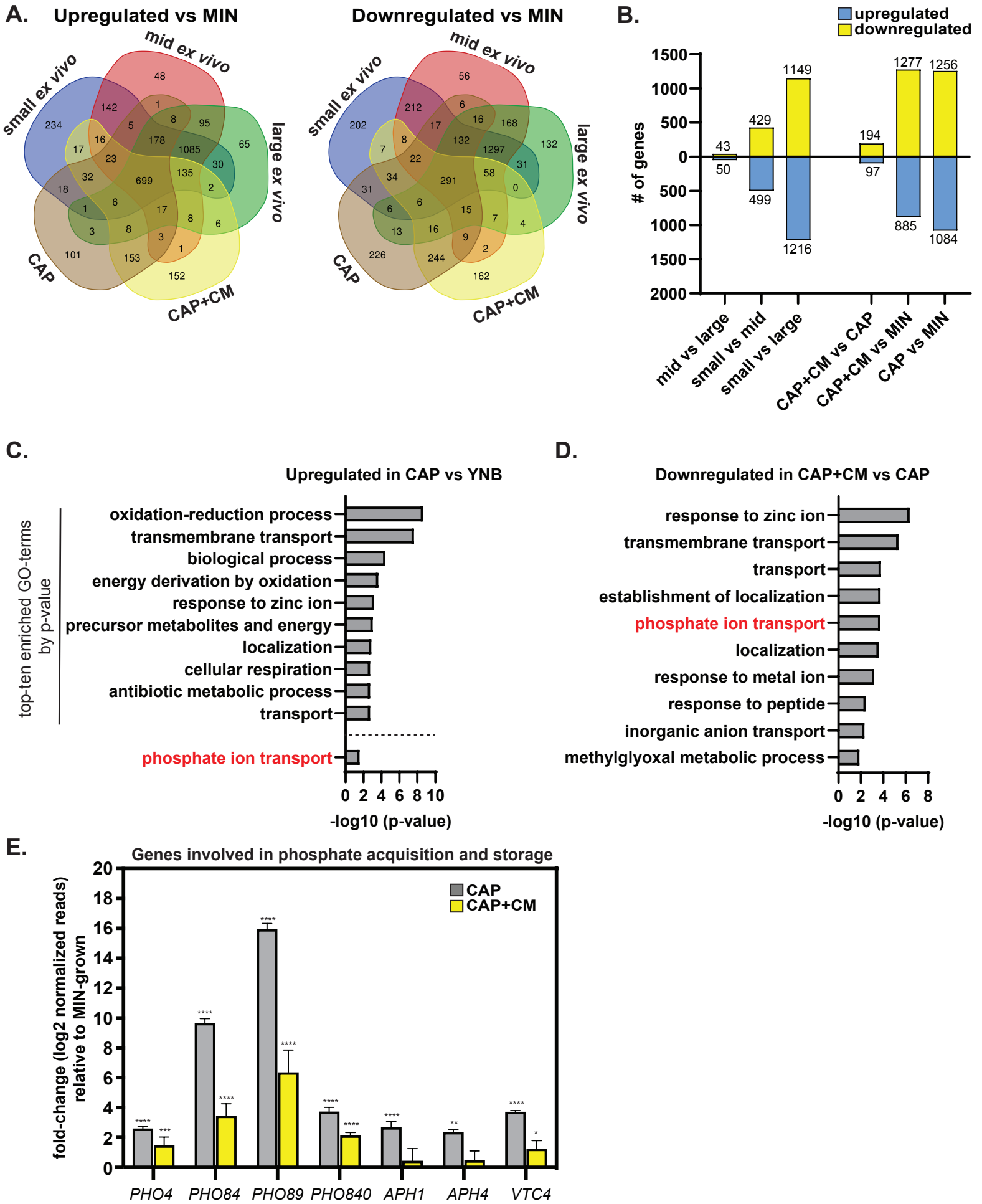
A.
Upregulated vs MIN
Downregulated vs MIN
small ex vivo
mid ex vivo
large ex vivo
CAP
CAP+CM
B.
upregulated
downregulated
# of genes
mid vs large
small vs mid
small vs large
CAP+CM vs CAP
CAP+CM vs MIN
CAP vs MIN
C.
Upregulated in CAP vs YNB
top-ten enriched GO-terms by p-value
oxidation-reduction process
transmembrane transport
biological process
energy derivation by oxidation
response to zinc ion
precursor metabolites and energy
localization
cellular respiration
antibiotic metabolic process
transport
phosphate ion transport
-log10 (p-value)
D.
Downregulated in CAP+CM vs CAP
response to zinc ion
transmembrane transport
transport
establishment of localization
phosphate ion transport
localization
response to metal ion
response to peptide
inorganic anion transport
methylglyoxal metabolic process
-log10 (p-value)
E.
Genes involved in phosphate acquisition and storage
CAP
CAP+CM
fold-change (log2 normalized reads) relative to MIN-grown
PHO4
PHO84
PHO89
PHO840
APH1
APH4
VTC4

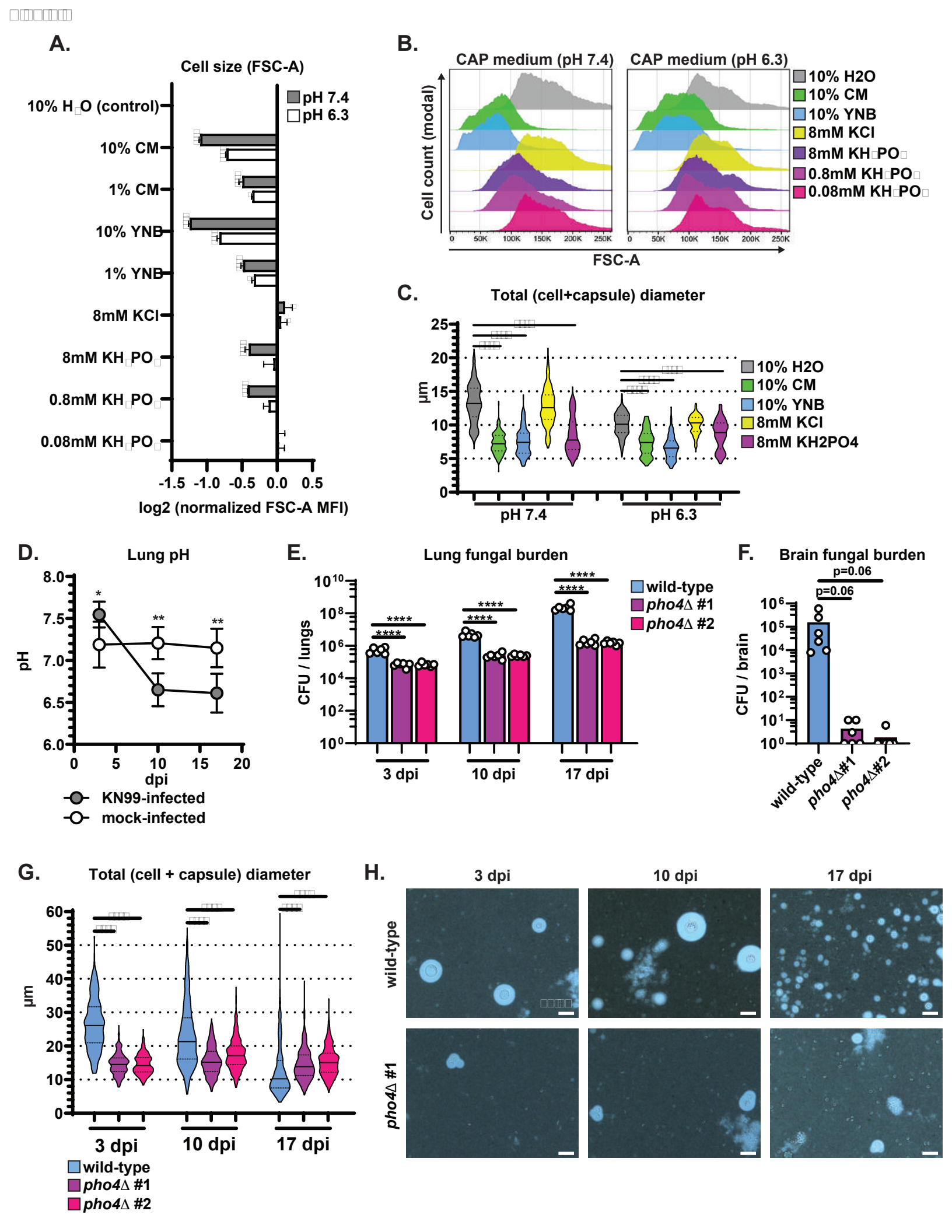
A.
Cell size (FSC-A)
pH 7.4
pH 6.3
10% H2O (control)
10% CM
1% CM
10% YNB
1% YNB
8mM KCl
8mM KH2PO4
0.8mM KH2PO4
0.08mM KH2PO4
-1.5 -1.0 -0.5 0.0 0.5
log2 (normalized FSC-A MFI)
B.
CAP medium (pH 7.4)
CAP medium (pH 6.3)
Cell count (modal)
FSC-A
10% H2O
10% CM
10% YNB
8mM KCl
8mM KH2PO4
0.8mM KH2PO4
0.08mM KH2PO4
C.
Total (cell+capsule) diameter
µm
10% H2O
10% CM
10% YNB
8mM KCl
8mM KH2PO4
pH 7.4
pH 6.3
D.
Lung pH
pH
dpi
KN99-infected
mock-infected
E.
Lung fungal burden
CFU / lungs
wild-type
pho4Δ #1
pho4Δ #2
3 dpi
10 dpi
17 dpi
F.
Brain fungal burden
p=0.06
p=0.06
CFU / brain
wild-type
pho4Δ#1
pho4Δ#2
G.
Total (cell + capsule) diameter
µm
3 dpi
10 dpi
17 dpi
wild-type
pho4Δ #1
pho4Δ #2
H.
3 dpi
10 dpi
17 dpi
wild-type
pho4Δ #1